Titre: Title:	On Delamination Crack Detection in Carbon Fiber Reinforced Polymers Using Electrical Impedance Tomography and Supervised Learning
Auteur: Author:	Augustin Schmidt
Date:	2018
Type:	Mémoire ou thèse / Dissertation or Thesis
Référence: Citation:	Schmidt, A. (2018). On Delamination Crack Detection in Carbon Fiber Reinforced Polymers Using Electrical Impedance Tomography and Supervised Learning [Mémoire de maîtrise, École Polytechnique de Montréal]. PolyPublie. https://publications.polymtl.ca/3710/

URL de PolyPublie: PolyPublie URL:	https://publications.polymtl.ca/3710/
Directeurs de recherche: Advisors:	Serge Prudhomme, & Marc Laforest
Programme: Program:	Maîtrise recherche en mathématiques appliquées

UNIVERSITÉ DE MONTRÉAL

ON DELAMINATION CRACK DETECTION IN CARBON FIBER REINFORCED POLYMERS USING ELECTRICAL IMPEDANCE TOMOGRAPHY AND SUPERVISED LEARNING

AUGUSTIN SCHMIDT
DÉPARTEMENT DE MATHÉMATIQUES ET DE GÉNIE INDUSTRIEL
ÉCOLE POLYTECHNIQUE DE MONTRÉAL

MÉMOIRE PRÉSENTÉ EN VUE DE L'OBTENTION
DU DIPLÔME DE MAÎTRISE ÈS SCIENCES APPLIQUÉES
(MATHÉMATIQUES APPLIQUÉES)
NOVEMBRE 2018

UNIVERSITÉ DE MONTRÉAL

ÉCOLE POLYTECHNIQUE DE MONTRÉAL

Ce mémoire intitulé :

ON DELAMINATION CRACK DETECTION IN CARBON FIBER REINFORCED POLYMERS USING ELECTRICAL IMPEDANCE TOMOGRAPHY AND SUPERVISED LEARNING

présenté par : SCHMIDT Augustin
en vue de l'obtention du diplôme de : Maîtrise ès sciences appliquées
a été dûment accepté par le jury d'examen constitué de :

M. ANJOS Miguel F., Ph. D., président
M. PRUDHOMME Serge, Ph. D., membre et directeur de recherche
M. LAFOREST Marc, Ph. D., membre et codirecteur de recherche
M. ADJENGUE Luc, Ph. D., membre

ACKNOWLEDGEMENTS

I would like to express my deepest gratitude to my advisors, Professor Serge Prudhomme and Professor Marc Laforest, for giving me this opportunity. Thank you for your patience and for everything you taught me. To Charly, thank for helping me with the numerical implementation. To Louis, thank for generating endless data points. It has been a pleasure to work with you. To Kenan, Antonin, and Elham, for your precious remarks.

Last but no least, thank to my parents for always being there to support me.

RÉSUMÉ

L'usage des Polymères Renforcés en Fibres de Carbone (PRFC) s'est répandu grâce notamment à leur important rapport résistance/poids, leur résistance à la corrosion et à la fatigue, et à la flexibilité qu'ils permettent lors de la conception, par rapport aux métaux. Ils sont composés de plaques de matrice polymère, renforcées par des fibres de carbone, qui peuvent être empilées et orientées arbitrairement de façon à atteindre les propriétés mécaniques désirées. En revanche, du fait de leur anisotropie mécanique élevée, les PRFC possèdent des modes de rupture qui leur sont propres. En particulier, la fatigue du matériau et un impact à basse énergie peuvent se traduire par le phénomène de délaminage, soit le décollement des plaques du matériau. Comme cette dégradation ne peut pas être détectée par inspection visuelle, la fiabilité des structures en PRFC s'en trouve réduite. Il est donc essentiel de développer une méthode automatique de détection du délaminage. Plusieurs techniques non-destructives existent déjà, parmi lesquelles figurent les ultrasons, les fibres optiques, les ondes de Lamb et les courants de Eddy. Cependant, la plupart de ces méthodes requièrent l'utilisation de capteurs coûteux et ne peuvent être appliquées lors de l'opération de l'appareil, ou nécessitent l'intervention sur place de personnel qualifié.

La Tomographie d'Impédance Électrique (TIE) a été envisagée pour la détection du délaminage en raison de son faible coût et de sa capacité à fournir des informations en temps réel sur la santé du matériau. Cette méthode consiste à reconstituer une carte de la conductivité d'un matériau en injectant des courants et en mesurant les différences de potentiel résultantes. Cependant, d'importantes incertitudes demeurent dans l'estimation de la position et de la taille du délaminage. Il est donc nécessaire de développer un outil qui permette, d'une part, de déterminer les mesures qui apportent le plus d'information vis-à-vis des paramètres du délaminage, et d'autre part, de tirer de ces mesures une estimation stable de ces paramètres. Dans ce document, nous étendons les méthodes d'apprentissage supervisé au traitement des données de TIE.

L'objectif général est l'optimisation de la configuration des électrodes pour l'application de la TIE à la détection de délaminage dans les PRFC. Ce projet s'articule en deux étapes. Dans un premier temps, il faut comprendre et formuler le modèle mathématique associé au problème direct ; nous reprenons le modèle d'électrode proposé par Somersalo et al. [41]. Cela implique aussi de caractériser et paramétrer le délaminage, ainsi que d'identifier les erreurs associées au modèle et aux mesures expérimentales. Cette étape mène à la génération de données synthétiques de mesures de potentiels à l'aide d'un logiciel d'éléments finis. Lors

de la deuxième phase, le problème inverse est abordé du point de vue de la classification binaire, l'inférence portant sur la présence de délaminage. Un bruit multiplicatif Gaussien est ajouté aux tensions mesurées. Plusieurs algorithmes issus de l'apprentissage automatique sont utilisés : la méthode des forêts aléatoires, la méthode des plus proches voisins, et la méthode des machines à vecteurs de support. Nous utilisons la performance de ces algorithmes en fonction des paramètres expérimentaux pour comprendre les relations existantes entre ces derniers. Nos résultats indiquent qu'une forte anisotropie ne rend pas toujours les prédictions plus difficiles ; cela peut même donner lieu à de meilleures prédictions lorsque l'espacement des électrodes est très supérieur à l'épaisseur du matériau. Ceci nous pousse à recommander des recherches plus approfondies au sujet de l'influence jointe des paramètres géométriques et électriques du matériau sur le positionnement optimal des électrodes.

ABSTRACT

Materials made of Carbon Fiber Reinforced Polymer (CFRP) are increasingly used in various engineering domains due to their high strength-to-weight ratio. However, they are subject to delamination, a mode of failure which can cause layers to separate. Since this type of failure is not visually observable, detection with non destructive testing is essential. The aim of Electrical Impedance Tomography is to reconstruct the conductivity distribution of a medium by injecting current through electrodes and measuring resulting voltages. More precisely, in the context of damage detection, the aim is to detect voltages anomalies that betray the presence of delamination. Research has already been done about statistical inference on delamination size and location. However, the inverse problem was always tackled from a regression point of view, and its study failed to provide insights about the joint influence of measurement noise and samples properties, such as geometry and electrical conductivity anisotropy, on the prediction performance. In this document, we generate synthetic data using a finite element software and borrow algorithms from the supervised learning field for the solution of the inverse problem. We study the impact of anisotropy, electrode positioning, and measurement noise on the prediction performance in a classification setting. We also show that cavities are easier to detect than delamination. Our results indicate that high anisotropy might not necessarily make inferring the presence of delamination more difficult. This leads us to recommend further research on the joint influence of geometry and anisotropy on optimal electrode spacing.

TABLE OF CONTENTS

LIST OF TABLES

LIST OF FIGURES

LIST OF ACRONYMS

AIC	Akaïke Information Criterion
BIC	Bayesian Information Criterion
CART	Classification and Regression Trees
CEM	Complete Electrode Model
CFRP	Carbon-Fiber Reinforced Polymer
EI	Effective Independence
EIT	Electrical Impedance Tomography
ERT	Electrical Resistance Tomography
FEA	Finite Element Analyses
FEM	Finite Element Method
FIM	Fisher Information Matrix
k-NN	k-Nearest Neighbors
NDE	Non-Destructive Evaluation
OOB	Out-Of-Bag
PCA	Principal Component Analysis
PDE	Partial Differential Equations
QI	Quasi-isotropic
SVD	Singular Value Decomposition
SVM	Support Vector Machine

CHAPTER 1 INTRODUCTION

CFRP laminates are increasingly used in various engineering fields due to their high strength to weight ratio. However, they are subject to delamination, a mode of failure which can cause layers to separate. Since this type of failure is not visually observable, detection with non-destructive testing is essential. The aim of EIT is to reconstruct the conductivity distribution of a medium by injecting current through electrodes and measuring resulting voltages. Our objective is to assess whether EIT can be used for detection of delamination between plies of a laminated composite. In other words, we want to design an algorithm that recognizes patterns that betray the presence of damage.

1.1 Context and Definitions

The subject of the present document deals with the monitoring of delamination in composites using EIT data. CFRP laminates are stacks of several laminae. Each lamina is composed of carbon fibers aligned in a single direction and held together by a binding polymer, which is often a thermoset resin such as epoxy. The laminas are stacked in different directions to obtain the desired mechanical properties.

Because of the brittle nature of the matrix material, failure modes in CFRP include intralaminar matrix cracking and interlaminar *delamination* cracks, caused by material fatigue and low energy impacts. Delaminations are impossible to detect from visual inspection and yield uncertainties about the material state. An efficient and reliable non destructive testing method is therefore needed. Several methods already exist: among them are ultrasounds, optic fibers, Lamb waves and Eddy currents [21]. However, those methods either require expensive sensors or cannot be used during operation (in flight, for example) and need the intervention of highly qualified personnel on site.

EIT is envisioned for delamination detection because of its low cost and its potential to yield real time information. This method consists in recovering the conductivity map of a material by injecting currents and measuring resulting voltages on the boundary using a network of electrodes. It has already been applied with success in medical imagery and geophysics [35], but the low thickness and high anisotropy of the CFRP make it difficult to use it for delamination detection [40]. The electrical conductivity of the CFRP is exclusively due to the highly conductive carbon fibers, the polymer matrix being an electric insulator. The conductivity observed in the directions normal to the fibers is caused by fiber interaction, due

to fiber waviness. As a consequence, the ratio of the conductivities in the fiber and normal to fiber directions lies well above 10: this ratio is about 25 for a 62% fiber volume fraction, and can be much higher for a lower volume fraction [44]. Since no fiber fracture is involved in a delamination, resistance changes are likely caused by reduction in the number of electrical conduction points between fibers due to ply separation. These changes are relatively small and hard to detect. A robust method remains to be developed to efficiently detect and locate delamination cases in CFRP using EIT.

In this document, it is assumed that the injected currents are at low frequencies, so the quasi-static approximation to the electric potential distribution can be used. This approximation allows us to reduce Maxwell's equation to a Laplace's equation (Cheney et al., 1999). The latter is linear and symmetric with respect to the injected currents, which lets us use fewer electrode injection schemes to gather the necessary data. Gathering real measurements data is a long, tedious and expensive process, so we propose to generate synthetic data using a finite element software: the modelization problem, or forward problem, is run multiple times to generate these voltage measurement data from varying values of the delamination parameters.

EIT is the problem that consists of recovering the material conductivity from these boundary voltage measurements. It is an *inverse* problem. As stated by Tarantola [42], "the inverse problem consists of using the actual results of some measurements to infer the values of the parameters that characterize the system". Here, the parameters that characterize the system are the size and location parameters of the delamination. However, the inevitable loss of information that happens during the measuring process makes EIT an *ill-posed* problem. A *well-posed* problem was defined by Hadamard [23] as a problem that consists of finding a solution of a mathematical model of a physical phenomenon that satisfies the three following properties: a solution exists, it is unique, and the solution's behavior changes continuously with the initial conditions. Problems that are not well-posed in the sense of Hadamard are termed ill-posed. Although the forward problem has a unique solution, given complete model data, the inverse problem only has partial data and hence more than one solution to the forward problem can satisfy the incomplete data available to the inverse problem. The EIT problem thus transgresses Hadamard's second property of a well-posed problem. Moreover, the remaining information is blurred by the noise inherent to the measurement process, and by limited numerical accuracy. We remark that in practice, delamination detection may be difficult to achieve with electrodes placed on one side of the laminate only [6]. One way to ease the parameter identification task is to place electrodes on both sides of the composite structure [18].

Due to the intrinsic difficulties of solving the EIT inverse problem, we propose in this work to use tools of machine learning in order to tackle the EIT problem on CFRP. A machine learning algorithm is "an algorithm that is able to learn from data" [22]. As stated by Mitchell [33], "a computer program is said to learn from experience E with respect to some class of tasks T and performance measure P, if its performance at tasks in T, as measured by P, improves with experience E". Machine learning enables computers to act and make data-driven decisions rather than being explicitly programmed to carry out a certain task. The present document is a preliminary study of the feasibility of damage detection in CFRP using EIT combined with supervised learning. The methodology described in the following chapters can also be extended to other inverse problem applications.

1.2 Literature review

EIT has been widely examined in the literature for detecting anomalies inside electric conductive bodies. We begin with the literature review of the modeling of the forward problem, before highlighting some problems specific to CFRP. We then review statistical tools that have been considered by other researchers for the solution of the inverse problem and provide an overview of some methods from the machine learning field.

1.2.1 EIT for damage detection in CFRP

Delamination in CFRP can grow quickly and cause structure failure. For that reason, they must be detected early. Giurgiutiu [21] provides a survey of Non-Destructive Evaluation (NDE) methods for laminated composites. Several NDE techniques are being studied for delamination detection. Among them are ultrasonics [5], thermography [49], radiography [16], electromagnetic testing [20], acoustic emissions [30], modal analysis [50], and electric resistance based methods. The latter use carbon fibers as sensors to detect electric resistance changes caused by the presence of delamination. Electrode attached on the composite surface are used to inject electric current and to measure resulting potential differences. We provide an overview of the available literature that addresses the modeling of the forward problem, the difficulties encountered in applying Electrical Resistance Tomography (ERT) to CFRP, and the statistical tools investigated for the inverse problem.

Modeling of the forward problem

Modeling of the forward problem has been extensively addressed since the 1980s, beginning in the medical field. Barber and Brown [3] first used electrodes to monitor the changes of

conductivity inside the human body. Somersalo et al. [41] proved the existence and uniqueness of the Complete Electrode Model (CEM). Using this model, they were able to predict experimentally measured voltages to within 0.1 percent, using a water-filled tank. Fouchard et al. [19] showed how to implement the CEM using Comsol Multiphysics.

Difficulties with CFRP

Wang and Chung [47] found that through-thickness electrical resistance measurements could be used to sense delamination in real-time during fatigue. Todoroki et al. [44] measured the effect of fibre volume fraction on electric conductance of CFRP laminates, and found experimentally that electric conductances in the transverse direction and thickness direction increase significantly with the fiber volume fraction. He also observed that delamination detection using the electric resistance change method is harder, for lower electric conductance in the thickness direction, i.e. when fiber volume fraction is low. However that study did not provide an electrical anisotropy threshold for delamination detection.

Schueler et al. [38] found that electrode positions must be changed in high anisotropy situations, and recommended using greater electrode density in the direction perpendicular to carbon fibers. Angelidis and Irving [2] found that delamination could be detected only when the surface current flow was parallel to the fiber direction and that surface potential fields are most sensitive to delamination damage located in the interface between the top and second laminae. They also observed that damaged areas consist of fiber breaks and intra laminar cracks as well as inter laminar delaminations, and concluded that the influence of the additional failure modes must be included in models before accurate prediction is achieved.

An analysis of potential measure sensibility to tranverse cracks in CFRP in presented in Selvakumaran et al. [40]. Recent work has allowed us to identify the limits of data from a numerical model when compared to data from a real experiment [6].

Statistical methods

Todoroki [43] found that response surfaces with quadratic polynomials are more efficient than artificial neural networks as an inverse problem tool for delamination detection. Then Todoroki et al. [45] used response surfaces to infer delaminations size and location from Finite Element Method (FEM) data and found that standardization of measured electrical resistance changes improves the prediction accuracy. Iwasaki and Todoroki [26] used the same method to detect delamination using experimental data from artificial delamination on real cross-ply and quasi-isotropic laminates. However these studies did not assess the impact of noise on

inference on the delamination size and location. They also did not provide a lower bound on the minimum number of samples needed to obtain satisfying prediction results, since they used a fixed number of finite element analysis samples (193 exactly). These experiments only concerned shallow delaminations, i.e. delaminations located between the 1st and 2nd plies from the electrodes.

Kammer [28] introduced the Effective Independence (EI) method for selecting an optimum set of sensor locations for the identification of a set of target vibration modes using finite element models, in the field of structural dynamics. Escalona-Galvis et al. [17] used this method to perform optimum electrode pair selection for ERT based damage detection using the two-probe method. They generalized this technique in Escalona-Galvis et al. [18] for the four-probe and multi-probe resistance methods. They also confirmed that using electrodes on both sides of the laminate provides better damage identification than using electrodes on one face only, and further stated that the most informative voltage measurements were that of neighboring electrodes. Some hypothesis were confirmed by the results found in Escalona-Galvis et al. [18] and Montiel [34]. However, this work was not used as a reference for our study since we discovered it during the summer of 2018.

While damage detection in CFRP using EIT has been studied, other methods are still preferred in the industry due to its lack of robustness. Our objective here is an attempt at improving its capabilities by coupling it with algorithms from the machine learning field. While artificial neural networks and response surfaces have been investigated for use in EIT field, many machine learning algorithms have yet to be studied for delamination detection. Also, to the best of our knowledge, EIT has not been studied from a classification point of view.

1.2.2 Machine learning

With the development of computers and the subsequent fall of computing price, a lot of attention has been given to the design of computer-intensive statistical methods since the 1950s. Rosenblatt [36] first published an example of a classification algorithm. Samuel [37] coined the tern “machine learning”. Numerous algorithms and variants of these were subsequently developed. Our study will focus on the k-Nearest Neighbors (kNN), the random forest, and the Support Vector Machine (SVM) algorithms, as they are some of the most popular and effective methods currently available.

The k-Nearest-Neighbor rule [11] is one of the oldest and simplest methods for pattern classification. It assigns to an unclassified point the class most significantly represented among vote by its k nearest neighbors in the training set. It is possible to show that asymptotically

the error rate of the k-NN rule is bounded by twice the Bayes rate.

Breiman [7] introduced Classification and Regression Trees (CART). Efron [14] introduced the bootstrap. Both were later combined in Breiman [8]. The most popular random forest algorithm appeared in Breiman [9]. Liaw et al. [31] provides an R interface to the random forest method, which we used.

Support Vector Machines were introduced by Cortes and Vapnik [10]. The SVM algorithm separates classes by constructing linear boundaries in a transformed version of the feature space. Meyer and Wien [32] provides an R interface to the C++ support vector machine library which will be used in our study.

1.3 Goals

The overall goal of this study is to define the feasibility criteria, i.e. the domain of experimental parameters space in which we can detect delaminations using EIT data with sufficient accuracy. This goal encompasses the following specific objectives:

- Determine which machine learning algorithm is best suited for detecting the voltage anomalies that betray the presence of damage in laminated composites. We will need to assess global range of accuracy, misclassification errors specific to certain algorithms, and improved accuracy for specific subsets of problems;

- Evaluate how many training samples are required to achieve a near optimal prediction accuracy. If each sample is expensive, the feasibility of real world delamination detection might be compromised if e.g. thousands of samples are needed to obtain sufficient accuracy. Thus damage detection must not only be theoretically feasible but also necessitate a reasonable amount of data. The asymptotic behavior of the test error will be monitored for that purpose;

- Point out the differences between detection of delaminations and other failure modes. Delaminations are notoriously hard to detect, in comparison with damages such as intra laminar cracks which cause fiber breakage. In this study small cavities will be used to represent loss of conductivity caused by fiber breakage;

- Perform optimal experimental design. We want to identify the electrode positions and current patterns that provide the most information about the delamination. The electrodes will be located on both sides of the laminate, since in our experience [6] the information provided by electrodes placed on one side only is insufficient. The

distribution of the electric potential is provided by a linear model and few electrodes are used (four on the two-dimensional experiment), so we can afford to use all linearly independent current patterns (maybe not on the 3D model). As some work has already been done about the selection of the optimal current injection when electrodes are at fixed positions [17], the study will focus on choosing the optimal electrode positions.

In order to simplify the study, but without loss of generality, the analysis will be performed on simplified configurations of the laminated composite. Several parameters will be held fixed throughout this document, but will be assigned values that are nonetheless comparable to those found in other studies on the topic. The study will thus focus on the anisotropy level (ratio of the conductivities in the fiber direction and in the through thickness direction), and on the noise intensity.

1.4 Methodology and Hypothesis

The quality of the training data is the most important criterion of success of any machine learning algorithm. Taking this fact into account, this project can be decomposed in two main stages. The first concerns the definition and implementation of the forward problem. This stage implies gaining a solid understanding of the equations describing the electric potential distribution, and is necessary to produce synthetic data that are as close to real life data as possible. To begin with, the mathematical model of the forward problem must be studied. The equations that characterize the distribution of the electric potential are derived from Maxwell's equations under the hypothesis that the current is quasi-static. The CEM proposed by Somersalo et al. [41] is presented. Its weak formulation is derived and implemented in Comsol Multiphysics with the method proposed by Fouchard et al. [19]. The mathematical model for the delamination is also discussed and its parameters are identified: these parameters will be the ones to be inferred when solving the inverse problem. The convergence of the resulting finite element code is studied: the mesh must be fine enough so that the numerical errors remain inferior to the voltage perturbations incurred by the presence of a significant delamination, but the computational cost must remain low enough to be able to generate a lot a data. The set-ups for our case studies, including the choice of the number of electrodes, current injection patterns, and type of CFRP, are discussed. They are simplified as much as possible to limit the data generation cost, using repetitions in the geometry and the symmetry of the mathematical model with respect to injected currents. The work on the forward problem implementation allows us to generate synthetic data used for the training and testing of machine learning algorithms. These data take the form of a *feature matrix*, with each row containing the voltage values corresponding to a single delamination

parameter value.

The second stage is concerned with developing a method for solving the inverse problem. To begin with, several preprocessing steps are considered. The first step consists in adding noise to the measured voltages, to account for the measurement uncertainties on one hand, and the material uncertainty (randomness during manufacturing) on the other hand. Subsequent preprocessing steps transform the data, and can feed different representations of the data to the machine learning algorithms in order to ease the parameter identification task. Several common machine learning algorithms are then trained on the generated EIT data: the k-nearest neighbors, random forests, and support vector machines with radial basis kernel. In contrast to other researchers, we will treat the inverse parameter identification as a binary classification problem, with a positive prediction indicating the presence of harmful delamination. The accent is put on non-parametric methods, since the main goal is prediction instead of explanation. The performance results attained by machine learning methods are then leveraged to specify the subset of the experimental set-up parameters that allow us to find a solution with a reasonable accuracy. Apart from the training distribution on the delamination parameters, several parameters of the experimental set-up also have a profound impact on the performance of the algorithms. The noise intensity plays an important role since no detection is possible if it is greater than the voltages changes incurred by the presence of a significant delamination. As a consequence, the performance of the algorithms will be assessed with various noise intensities.

In this study, it is assumed that the electrode contact impedances are known. This is considered realistic in the context of an intelligent CFRP laminate with built-in electrodes. In other EIT applications, the electrode contact impedance must usually be inferred. For example, in cancer detection, there is a layer of unknown conductivity at the skin–electrode interface [13]. The through-thickness conductivity will be assumed constant at all points of the material, so this study also applies to intra-laminar cracks. In reality, inter-laminar delaminations are harder to detect than intralaminar cracks because a thin fiber free (matrix rich) zone is observed at ply-ply interfaces in real samples [44]. Another important parameter is the electrode density. The electrode density is defined as the ratio between the inter-electrodes distance and the laminate thickness. As mentioned earlier, electrodes will be placed on both sides of the laminate in the following analysis, as opposed to previous studies that examined the applicability of EIT to CFRP using electrodes placed on one side only. The electrode density will be held fixed throughout this document. An experimental design part will close the study, as the damage detection accuracy will be computed for several electrodes positions. Though the electrode density will remain fixed, an electrode *shift* parameter is introduced as in Beck et al. [4] to account for the positional shift between the upper and lower electrodes.

1.5 Outline

Chapter 2 is concerned with the data generation method. First of all, the mathematical model for the electric potential distribution is presented. It is justified based on preliminary experiments. At the end of the chapter, several case studies will be used to demonstrate our method. The first is based on delamination data generated using a simple two-dimensional geometry, and is used to get a good understanding of the problem and to test the code. The second experiment is similar to the first, except that delaminations are replaced by cavities.

Chapter 3 deals with how to leverage the EIT data to infer the delamination parameters using machine learning algorithms. It begins with a short introduction to basic machine learning concepts before embarking on the theme of data preprocessing. Three standard machine learning algorithms are then presented. The model selection problem is addressed at the end of this chapter.

Chapter 4 focuses on presenting the results and providing answers about the feasibility. Inference accuracy of the different algorithms is compared for several electrode positions and anisotropy levels. We attempt to give an answer about the amount of data necessary for successful damage detection for various failure modes. The delamination detection problem by EIT is very difficult, and many of our results confirm the difficulties others have identified in past studies, but this research additional information about what can and cannot be done.

CHAPTER 2 FORWARD PROBLEM

The efficiency of data analysis methods depends heavily on the quality of the data at hand. In other words, we need data that is representative of the true underlying population. We do not have the means to obtain real data, since it requires having access to specific instruments and experimental set-up. Instead we generated the data by numerical simulation. We need a mathematical model that yields numerical data that is close enough to real world data. In this chapter, we describe the mathematical model that governs the electric field in a damaged laminated composite, along with its implementation.

We have seen that much research has already been invested in accurate modelling of electric potential distribution in EIT context. In this chapter, we begin by presenting the model geometry and the equations of the Complete Electrode Model (CEM). We then go through the delamination parametrization and the difficulties encountered in implementing the CEM with the Finite Element Method (FEM). We end the chapter with the description of the simplified case studies that we will analyse thoroughly in the following chapters.

2.1 Mathematical model

The electrical potential u is governed by the Poisson equation resulting from the low frequency quasi-static approximation of Maxwell's equation:

$$\nabla \cdot (\sigma \nabla u) = 0, \qquad \text{in } \Omega, \tag{2.1}$$

where σ is the 3×3 conductivity tensor of a ply.

Let L be the number of electrodes, with E_ℓ the surface covered by the ℓ-th electrode. The current injecting condition on the electrode area is given by

$$\int_{E_\ell} n \cdot \sigma \nabla u \, ds = I_\ell, \qquad \text{on } E_\ell, \quad \ell = 1, 2, \ldots, L, \tag{2.2}$$

where $n \cdot \sigma \nabla u$ is the current density through the domain boundary. Equation (2.2) forces the integral of the current density on an electrode to equal I_ℓ, the inward current intensity on electrode ℓ.

The rest of the boundary acts as an insulator, i.e. we have

$$n \cdot \sigma \nabla u = 0, \qquad \text{on } \partial\Omega \setminus \bigcup_{\ell=1}^{L} E_\ell. \tag{2.3}$$

Let U_ℓ be the potential provided by the ℓ-th electrode and z_ℓ the contact impedance between the ℓ-th electrode and the composite. The potential jump at the electrode-composite interface is given by

$$u + z_\ell \, n \cdot \sigma \nabla u = U_\ell, \qquad \text{on } E_\ell, \quad \ell = 1, 2, \ldots, L. \tag{2.4}$$

Equation (2.4) involves z_ℓ, preventing the "shunting effect", i.e. the tendency of the current to take the shortest path between injecting electrodes by flowing exclusively through the closest electrode extremities [41]. z_ℓ can represent, for example, the impedance of the glue used to attach the electrode to the composite material under study, or the lack thereof. U_ℓ is constant on the ℓ-th electrode area (on electrode side), while u (on composite side) can vary considerably.

The existence and uniqueness of the solution is ensured by Kirchhoff's current law,

$$\sum_{\ell=1}^{L} I_\ell = 0, \tag{2.5}$$

and the specification of a potential ground:

$$\sum_{\ell=1}^{L} U_\ell = 0. \tag{2.6}$$

2.2 Parametrization

We now discuss the parametrization of the experiment. We start with the description of a typical geometry and of the conductivity parameters. We then characterize mathematically the delamination and introduce a simple parametrization for its identification. The parameters, and typical values when applicable, are summarized in Table 2.1.

2.2.1 Geometry

The following geometry is taken from preliminary experiments described in Billet et al. [6]. The composite sample used for our preliminary experiments is a quasi-isotropic laminate

Table 2.1 List of parameters for EIT experiment.

Symbol	Definition	Value	Source
Geometry			
w	Width of domain	150 mm	Billet et al. [6]
h	Thickness of domain	2 mm	Billet et al. [6]
L	Number of electrodes	16	Billet et al. [6]
$\lvert E_\ell \rvert$	Area covered by the ℓ-th electrode	7 mm $\times$ 7 mm	Billet et al. [6]
Δe	Distance between electrodes	27 mm, center to center	Billet et al. [6]
Electrical conductivity			
σ_0	Conductivity in fiber direction	5500 $\mathrm{S \cdot m}$	Todoroki et al. [44]
σ_{90}	Conductivity in in-plane, normal-to-fiber direction	203.5 $\mathrm{S \cdot m}$	Todoroki et al. [44]
σ_t	Conductivity in through-thickness direction	20.9 $\mathrm{S \cdot m}$	Todoroki et al. [44]
z_ℓ	ℓ-th electrode contact impedance	$10^{-4}\,\Omega \cdot \mathrm{m}^2$	[40]
Delamination			
$\{\xi_1, \xi_2\}$	In-plane coordinates of delamination center	$\{75, 75\}$ mm	Billet et al. [6]
ζ	Delamination height	1.75 mm	Billet et al. [6]
ρ	Delamination radius	25 mm	Billet et al. [6]

with stacking sequence $[0^\circ/45^\circ/90^\circ/-45^\circ]_s$. Each ply has thickness 0.25 mm. 16 electrodes are stuck on one side of the laminate. Figure 2.1 displays the composite dimensions as well as the electrode positions.

2.2.2 Laminate conductivity tensor

The homogenized orthotropic conductivities of a neat CFRP with a fiber volume fraction of 0.62 were chosen for the purpose of the preliminary simulations. These values were found in Todoroki et al. [44], who justified the use of homogeneous orthotropic conductivities as follows: "Since the diameter of a typical graphite fiber is much smaller than the size of FEM elements adopted here, the inhomogeneous orthotropic graphite/epoxy composite material is assumed to be a homogeneous orthotropic material for present FEM analysis".

2.2.3 Delamination

The previous section was concerned with introducing common values of orthotropic conductivities for an undamaged CFRP. Now we specify how delamination changes the electrical properties of the laminate. In a given new CFRP, fibers are not perfectly straight. Instead they are wavy, allowing multiple fiber to fiber contacts everywhere in the laminate, and thus allowing non zero conductivity in the normal to fibers plane. When a delamination appears between two laminae, they are locally separated, preventing electric current to flow through.

Though it may be possible that a real delamination only partially stops the current, we assume for simplification purposes that it is a perfect insulator. Mathematically, it means that the current density through the crack is zero, i.e. $\sigma\dfrac{\partial u}{\partial n} = 0$, where n is the direction perpendicular to the delamination, such that the electric current is forced to flow around the crack. In reality, delaminations can have complicated shapes, and can even be comprised of multiple tiny delaminations. We further simplify the study by imposing a circular shape, with radius ρ. The main motivation for such a delamination is that it should be artificially reproducible in a controlled environment by e.g. inserting a thin layer of teflon between two plies. A delamination can then be completely identified with only the following parameters:

- ξ_1, ξ_2 : delamination center in-plane coordinates;
- ζ : delamination height;
- ρ : delamination radius.

We should remark that all of our modeling choices were biased towards making the delamination either as easy to detect, or easier to detect, than a real delamination. Therefore,

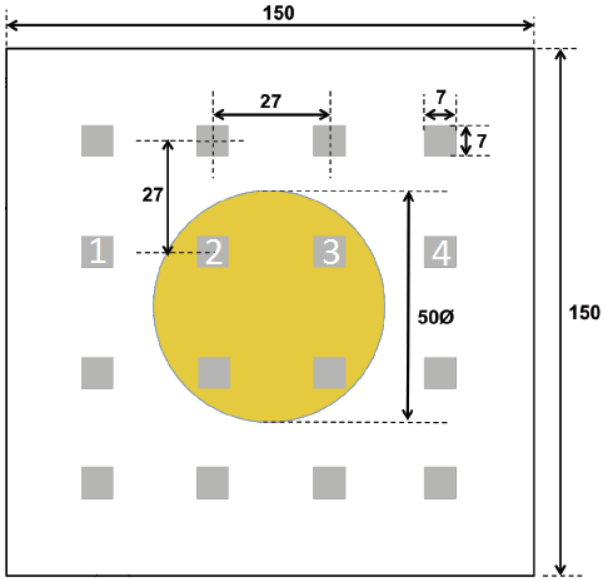

Figure 2.1 Geometry of the sample. All dimensions are expressed in [mm].

any conclusion about the detectability, through various means, will be an overestimate; in fact, this is the type of bias one would expect given the inherent complexity in the problem. Having defined the mathematical model for EIT with CFRP, we can now describe its implementation using the FEM.

2.3 Finite element simulation

This section is concerned with the implementation of the mathematical model presented in Section 2.1. We should note that the purpose of those simulations was to develop a numerical model for experiments referenced in the technical report Billet et al. [6].

We use the AC/DC module in COMSOL Multiphysics® to build the application. We begin by mentioning some issues encountered in the implementation, such as having to rewrite equation (2.4), the creation of a specific domain for each ply, and specific meshing. We then make some remarks about convergence and cost, and display preliminary results.

2.3.1 Boundary conditions

In COMSOL Multiphysics AC/DC module, the implementation of the Robin equation (2.4) is not straightforward. We thus chose to consider the alternative condition as derived in

Fouchard et al. [19]:

$$-n \cdot J = \frac{1}{z_\ell |E_\ell|} \left(z_\ell I_\ell - |E_\ell| u + \int_{E_\ell} u \, ds \right), \tag{2.7}$$

where $-n \cdot J$ is the electric current density on the ℓ-th electrode, and $|E_\ell|$ the area of the ℓ-th electrode.

The expression (2.7) is obtained as follows. If we integrate (2.4) on the area covered by one electrode, we obtain

$$\int_{E_\ell} (u + z_\ell \, n \cdot \sigma \nabla u) \; \partial\Gamma = U_\ell \, |E_\ell|, \tag{2.8}$$

and simplifying using (2.2), we get

$$\frac{1}{|E_\ell|} \int_{E_\ell} u \, \partial\Gamma + \frac{z_\ell \, I_\ell}{|E_\ell|} = U_\ell. \tag{2.9}$$

Replacing U_ℓ by the above expression in (2.4) and isolating the current density, we finally get

$$-n \cdot J = n \cdot \sigma \nabla u = \frac{1}{z_\ell \, |E_\ell|} \left(\int_{E_\ell} u \, \partial\Gamma + z_\ell \, I_\ell - |E_\ell| \, u \right) \tag{2.10}$$

that we can prescribe in Multiphysics as a Neumann condition.

2.3.2 Conductivity tensors

Since fiber direction changes with each ply, a specific domain must be created for each of them in order to assign them the appropriate conductivity tensors. The latter are summed up in Table 2.2. They are given relative to the coordinate system of the 0° ply.

Table 2.2 Conductivity tensor σ (in $\mathrm{S} \cdot \mathrm{m}$) for each ply orientation.

0°-ply	90°-ply
$\begin{bmatrix} 5500 & 0 & 0 \\ 0 & 203.5 & 0 \\ 0 & 0 & 20.9 \end{bmatrix}$	$\begin{bmatrix} 203.5 & 0 & 0 \\ 0 & 5500 & 0 \\ 0 & 0 & 20.9 \end{bmatrix}$
45°-ply	**-45°-ply**
$\begin{bmatrix} 2852 & 2648 & 0 \\ 2648 & 2852 & 0 \\ 0 & 0 & 20.9 \end{bmatrix}$	$\begin{bmatrix} 2852 & -2648 & 0 \\ -2648 & 2852 & 0 \\ 0 & 0 & 20.9 \end{bmatrix}$

2.3.3 Meshing

For the numerical simulation, the geometry is the same as that presented in Billet et al. [6]. We proceeded by first designing a 2D geometry, featuring the domains for the electrodes and the delamination region, by creating a triangulation of this 2D model with small elements near the electrodes and around the delamination boundary, and by extruding the latter by 0.25 mm in order to obtain the first ply. The complete geometry was eventually generated by repeating the extrusion process 8 times, i.e. one for each ply. This process yielded 17,936 prisms elements and 76,925 degrees of freedom for the entire model, shown in Figure 2.2.

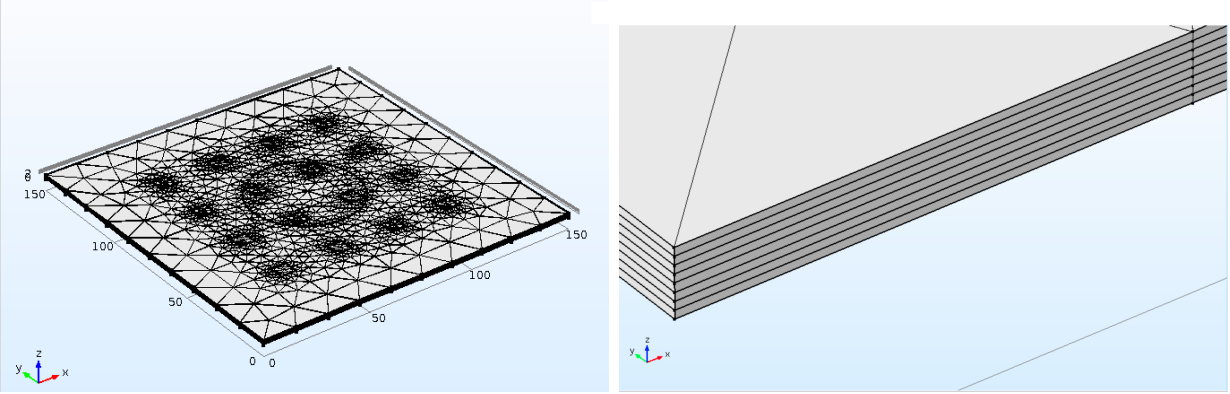

Figure 2.2 Meshing of the 8-ply quasi-isotropic laminate, using Comsol Multiphysics. The whole laminate is shown on the left, while a close-up on a corner is shown on the right.

2.3.4 Convergence study

A simple test case is considered here. It consists of the composite plate without delamination. The injected current is 10 mA for the upper left corner electrode. In order to satisfy Eq. (2.5), the injected current is -10 mA at the bottom right corner electrode. We assume that the contact impedance z_ℓ is the same for both electrodes, with value $10^{-4}\,\Omega\cdot\mathrm{m}^2$. A top-view of the results for the potential distribution on the electrode side is shown in Figure 2.3.

One hypothesis we made is to assume that U_ℓ is constant on the ℓ-th electrode, $\ell = 1, \ldots, L$. Since in Comsol Multiphysics this constraint is implemented indirectly using equation (2.7), we decided to check if it is verified after computation. The solution on the coarse mesh was unsatisfactory. The mesh was then modified in two ways. Firstly, we kept the refinement along the boundaries of the two active electrodes only. Secondly, we increased the number of elements in the ply below the electrodes in the normal direction to the ply. Figure 2.4 shows the resulting values of U across an electrode area. U seems to converge to a constant value

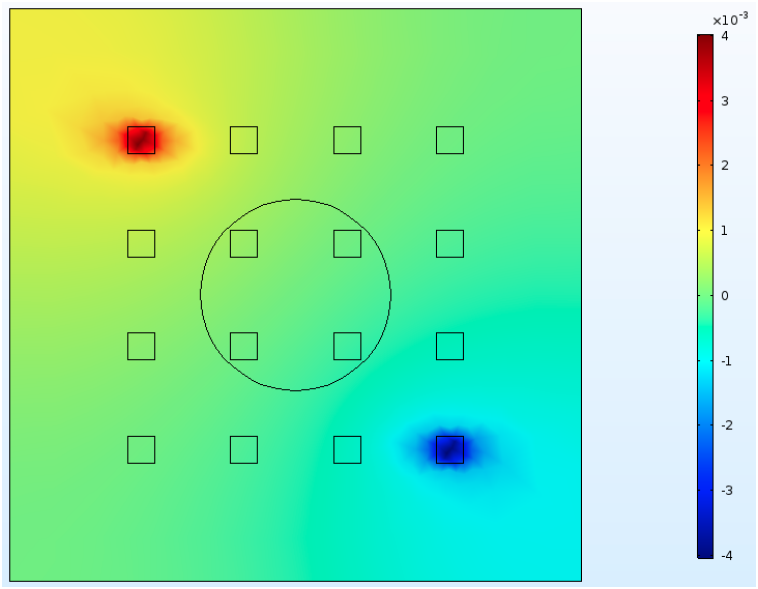

Figure 2.3 Electric potential on top surface obtained for the test case (with coarse mesh).

on the whole electrode area.

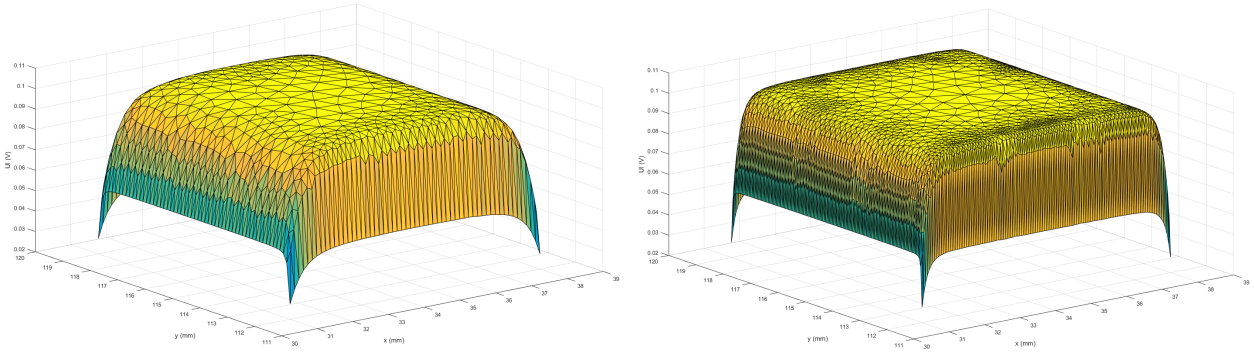

Figure 2.4 Influence of the number of elements in the normal direction to the ply. Left: 2 elements across ply. Right: 5 elements across ply.

The observation that the value of U_ℓ tends to converge to a constant led us to the next study. For different meshes, we calculated $\overline{U}_\ell$, the mean value of U_ℓ defined by:

$$\overline{U}_\ell = \frac{1}{|E_\ell|} \int_{E_\ell} U_\ell ds. \tag{2.11}$$

To verify the convergence of this quantity, we calculated the relative L^2-norm of the error:

$$\|U_\ell - \overline{U}_\ell\| = \frac{\left(\int_{E_\ell} \left(U_\ell - \overline{U}_\ell\right)^2 ds\right)^{\frac{1}{2}}}{\left(\int_{E_\ell} \overline{U}_\ell^2 ds\right)^{\frac{1}{2}}}, \tag{2.12}$$

where the constant value of $\overline{U}_\ell$ is taken from the most refined mesh. The results of the study are presented in Figure 2.5.

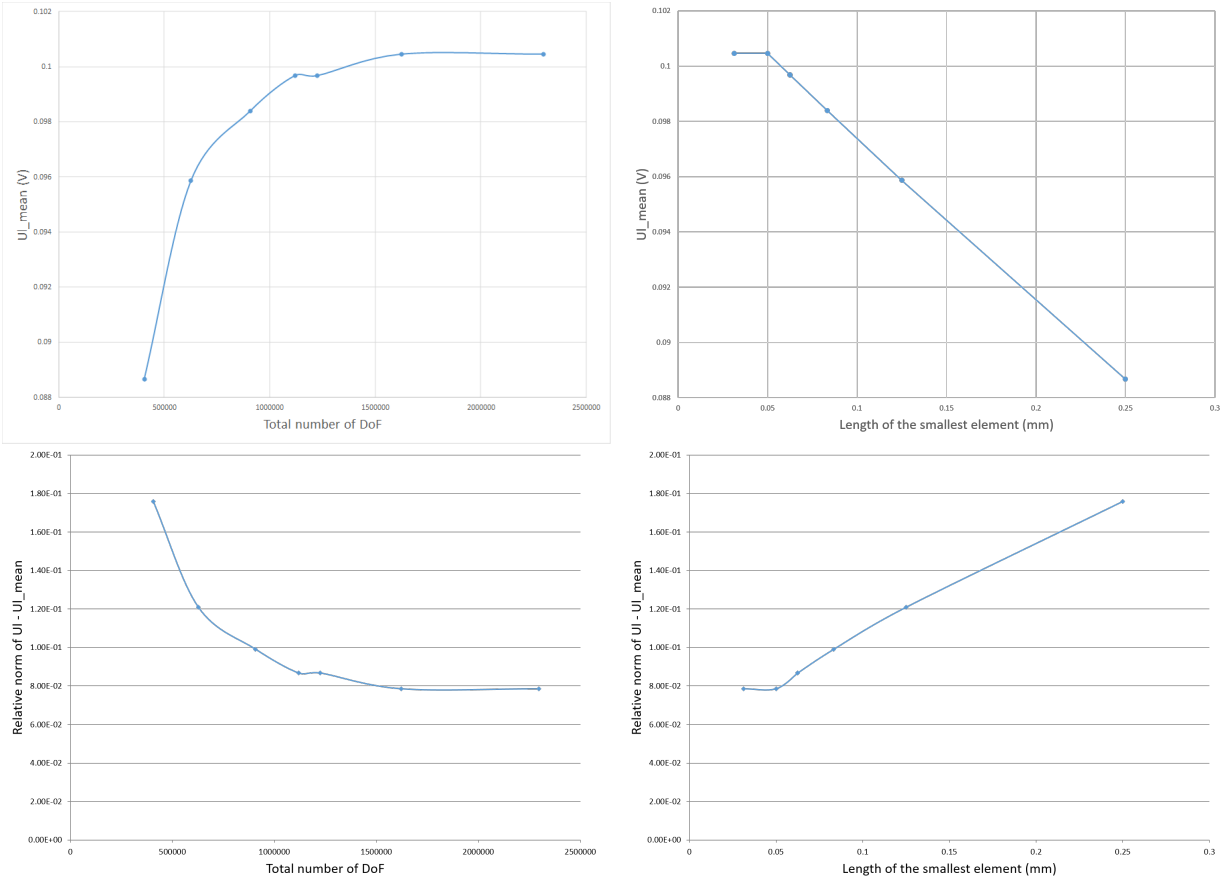

Figure 2.5 Results of convergence study. Top left: $\overline{U}_\ell$ vs total number of degrees of freedom. Top right: $\overline{U}_\ell$ vs length of smallest element in [mm]. Bottom left: relative error in U_ℓ vs total number of degrees of freedom. Bottom right: relative error in U_l vs length of smallest element [mm].

2.3.5 Example

As an example, we present the perturbation of the electric potential caused by the presence of a delamination. An artificial delamination with a diameter of 50 mm is introduced in the

laminate. Figure 2.7 shows the difference between solution u of an undamaged laminate and solution u_0 with defect in 2$^{\text{nd}}$ ply. These results are obtained using a mesh with $\sim 2.8 \times 10^6$ degrees of freedom (3 minutes of run time). A convergence study shows that the numerical errors are below 2%.

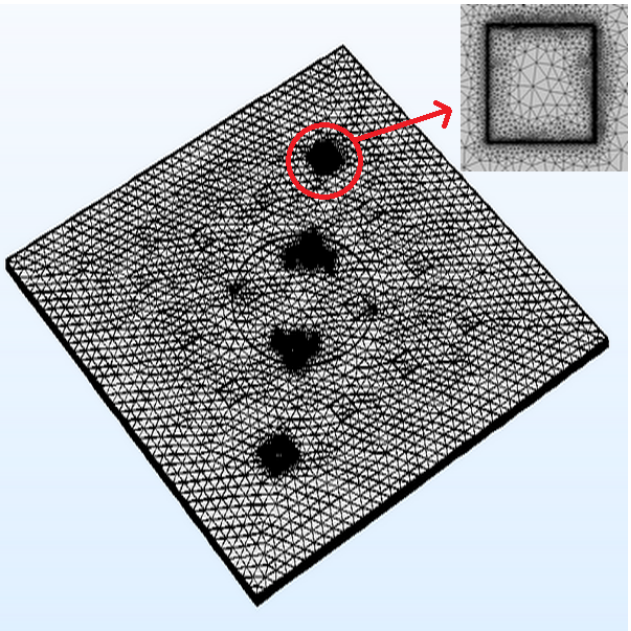

Figure 2.6 Geometry (150mm $\times$ 150mm $\times$ 2mm) and mesh with 2,800,000 DoFs.

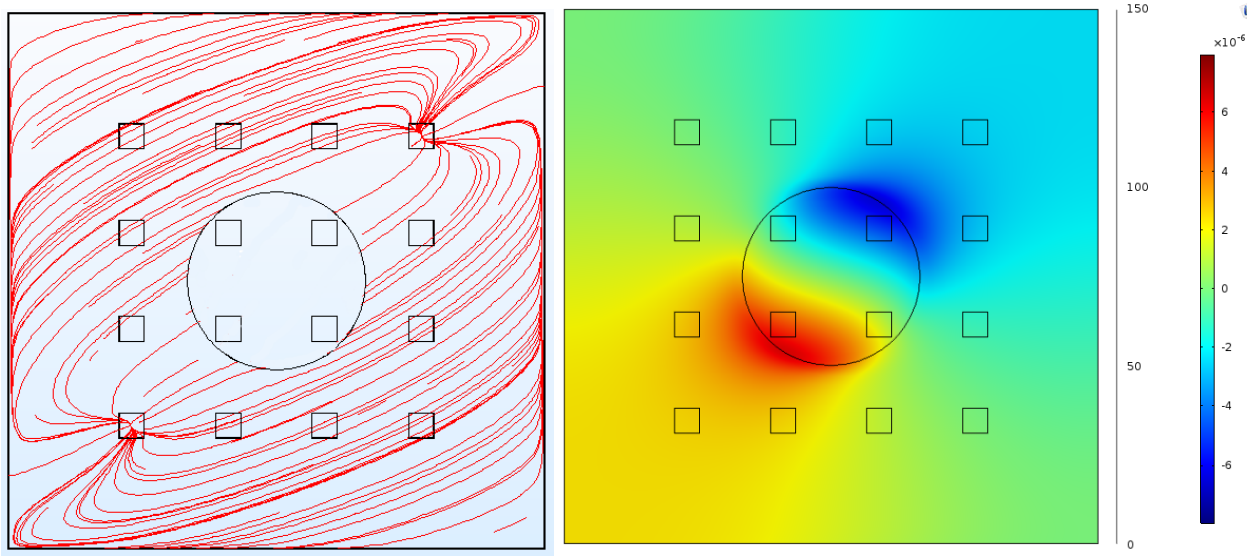

Figure 2.7 Left: streamlines of u_0 on the top of the 2$^{\text{nd}}$ ply. Right: $u - u_0$, the potential difference between undamaged laminate and laminate with delamination under 1$^{\text{st}}$ ply.

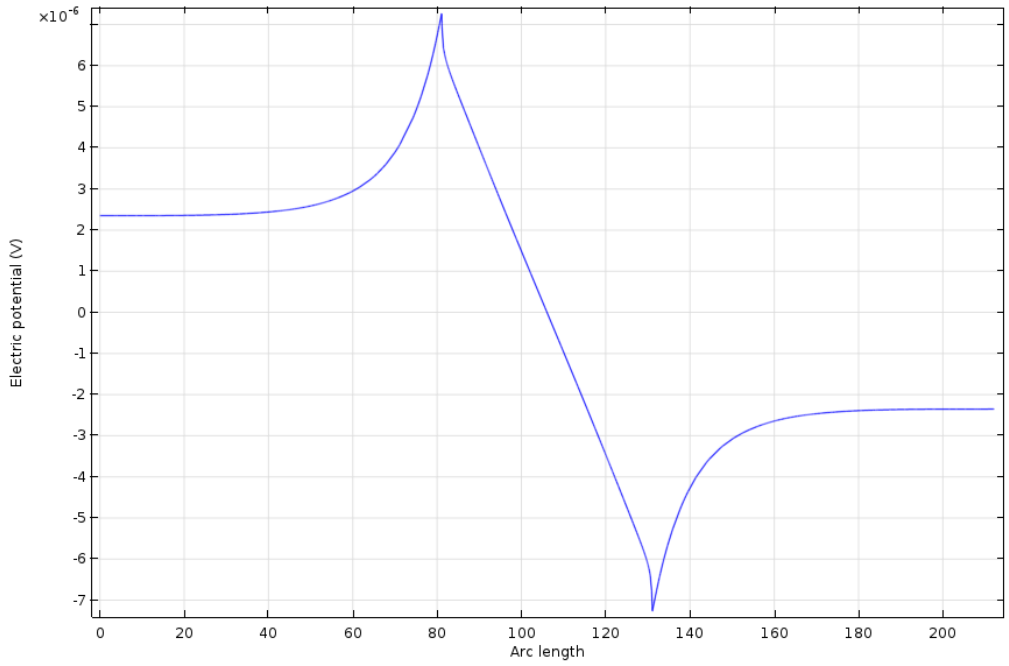

Figure 2.8 $u - u_0$, the potential difference between undamaged laminate and laminate with delamination under 1st ply, along the diagonal from bottom left to top right (see Figure 2.7). Relative voltage change on measuring electrodes is 1.34%.

2.4 Generation of surrogate data

Simple case studies will be considered to demonstrate the application of the method developed in this document. The objective is to define simple model problems on which we will be able to use the methods considered in this work and analyze a variety of test cases. Hence the effort will be centered on leveraging the symmetries of the mathematical model to find a geometry and a probability density function on the delamination parameters that are, on the one hand, as simple as possible to minimize the cost of data generation, yet general enough so the analysis can remain relevant for realistic configurations.

The first model uses a simple two-dimensional sample geometry, consisting of a single lamina. Having only a single lamina will allow us to better evaluate the effect of λ, the ratio between in-plane and through-thickness conductivities, on the classification performance in Chapter 4. The second model is the same as the first, except that delaminations are substituted by cavities.

2.4.1 2D experiment with delamination

First, we present a simple two-dimensional composite sample. We justify the choice of our example geometry.

Experimental setup Let us consider a two-dimensional composite consisting of a single lamina of infinite width, shown in Figure 2.9 with regularly spaced electrodes on each side. Using the symmetries and periodicity of the boundary data, it is argued that a generic 4-electrode two-dimensional example is sufficient to study the detectability of a delamination. That choice is also supported by the study of Escalona-Galvis et al. [18], who found that the most informative voltage measures were that of neighboring electrodes.

The detectability task is the same, whether the delamination is located between electrodes 1, 2, 5, and 6, or between electrodes 2, 3, 6, and 7. Furthermore, from our experience, if the delamination is located inside a polygon whose vertices consist of a group of four neighboring electrodes, e.g. electrodes 1, 2, 5, and 6, the information provided by electrodes farther from the delamination, e.g. electrodes 3 and 7, is negligible [6]. This observation was also made in Escalona-Galvis et al. [18] and Todoroki [43]. Hence an analysis conducted on a sample with two electrodes on each side should be sufficient to understand the behavior for a larger geometry and multiple electrodes.

Although we could also study the influence of the electrode size E_e and spacing E_{sp} on the detectability problem, we preferred to concentrate on the case where the electrodes on one side are shifted by a shift with length E_{sh}. Hence we will use the constant values from past experiments (preliminary studies), i.e. $E_e = 7$ mm and $E_{sp} = 20$ mm. If the electrode density was higher, the detectability would likely increase, so that our hypothesis of constant E_e and E_{sp} should not affect the applicability of the machine learning methods.

The sample must be much larger than the electrode spacing E_{sp}. This allows the electric current to flow well outside the zone between the electrodes, instead of being forced in that

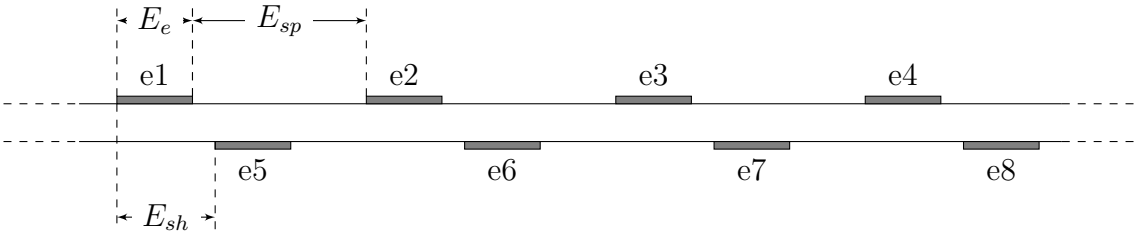

Figure 2.9 2D schematic representation of an infinite laminate.

zone, so as to simulate the "infinite lamina" situation. It also allows us to neglect edge effects. This allows us to conclude that a sample of 150 mm in width should be reasonable. The chosen lamina thickness is 2 mm; it is the same as the thickness of the whole laminate in our preliminary experiment. We fix the contact impedance z_ℓ to $10^{-4}\ \Omega \cdot \mathrm{m}^2$, based on the value seen in Selvakumaran et al. [40]. Although we have observed large variations in the published values, this order of magnitude is within the middle of the range of values we have found. Although it is well-known that the higher the contact impedance, the lower the detectability, since it causes the internal resistance changes to have a lower relative impact on the outer voltage increases, its influence on the results will not be studied in this work. A representation of the final geometry of the sample under study is shown in Figure 2.10.

Probability density functions of delamination parameters Let Θ be a vector containing all the delamination parameters, i.e. $\Theta^T = (\rho, \xi, \zeta)$, where ρ, ξ, and ζ are the delamination radius and the coordinates of the delamination center, respectively.

The probability density function for the parameters Θ must be chosen so that they are relevant to the cases of delaminations observed in practice. For example, some layers might be more susceptible to delamination, and delamination might often occur jointly with other defects. This is important because if the chosen distribution for Θ is far from its true distribution, the test error may be misleading. However, as no such data is available in the literature, we follow the usual scientific ansatz and choose a non informative (maximum entropy) distribution on the parameters.

Figure 2.11 shows the parametrization of the delamination. The delamination center location, parametrized by ξ and ζ, follows a uniform distribution inside the dotted rectangle,

$$\xi \sim \mathcal{U}\,(\xi_{min}, \xi_{max}),$$
$$\zeta \sim \mathcal{U}\,(h_{min}, h_{max}).$$

Since lamina thickness is often around 0.25 mm, we assume that delaminations are at least

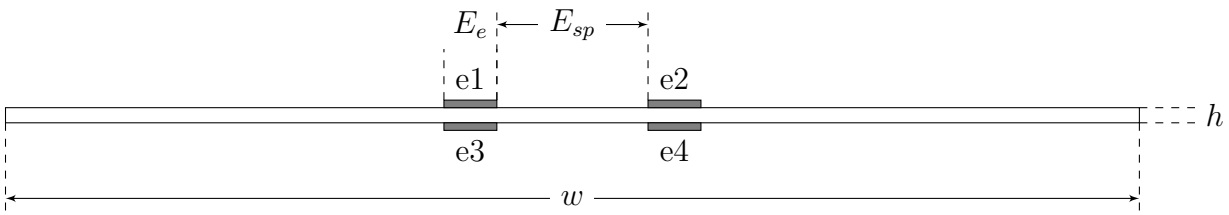

Figure 2.10 2D geometry. All dimensions are given in millimeters.

0.25 mm from the laminate surface. We choose a continuous uniform distribution instead of a discrete distribution for the delamination depth. The delamination radius ρ is drawn uniformly from 0 mm to $\rho_{max} = (E_e + E_{sp})/2 = 13.5$ mm, i.e.

$$\rho \sim \mathcal{U}(0, \rho_{max}).$$

ξ, ζ, and ρ are assumed independent. The forward problem described earlier then maps Θ to the voltages. The geometrical and electrical parameters used for the computation are summarized in Table 2.3.

The numbers of degrees of freedom for each configuration vary between 8,000 and 13,000 degrees of freedom, depending on the delamination size and position. It took approximately 90 minutes to generate data corresponding to 1,000 delaminations with COMSOL on a new but standard desktop.

Injection patterns Here, an injection pattern refers to the electric current intensities sent through the electrodes. It is represented by a vector I of length L, the number of electrodes, with each entry corresponding to a single electrode. A positive value indicates that the current flows in the inward direction, i.e. from electrode to composite. Hence we have

$$I = \begin{bmatrix} I_1 \\ I_2 \\ I_3 \\ I_4 \end{bmatrix} \qquad \text{where} \quad I_\ell = \int_{E_l} n \cdot \sigma \nabla u \, ds, \quad \ell = 1, 2, 3, 4. \tag{2.13}$$

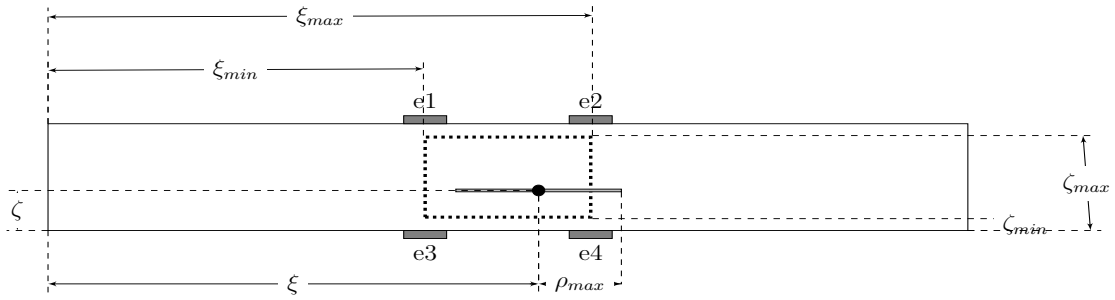

Figure 2.11 Delamination parameterization. Vertical dimensions are exagerated.

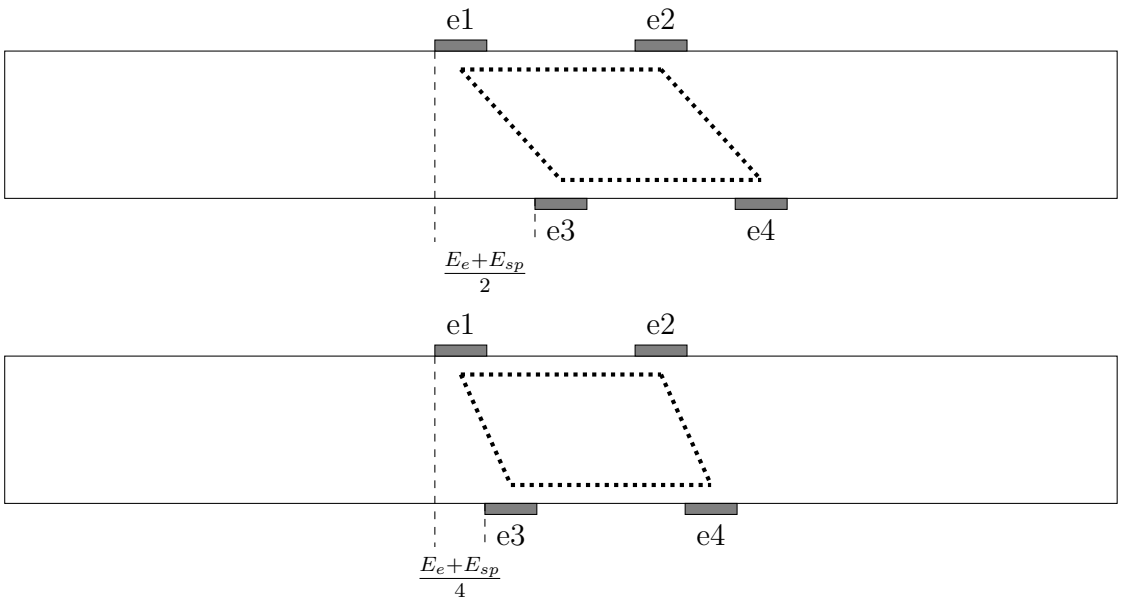

Figure 2.12 Prior constraints and electrode positions. Vertical dimensions are exagerated.

Table 2.3 2D experiment parameters list

Symbol	Definition	Value
Geometric parameter of the composite sample		
w	Composite sample width	150 mm
h	Composite sample thickness	2 mm
n	Number of laminæ	1
Delamination parameters		
ρ	Delamination radius	$0 < \rho < 13.5$ mm
ξ	Absciss of delamination center w.r.t. left side	$61.5 < \xi < 88.5$ mm (when $E_{sh} = 0$)
ζ	Delamination ordinate	$0.25 < \zeta < 1.75$ mm
Electrical conductivities and resistances		
σ_0	Conductivity in fiber direction	5 500 S · m
λ	Ratio of in-plane and through-thickness conductivities $\lambda = \frac{\sigma_0}{\sigma_t}$	$\lambda \in \{1, 10^1, 10^2, 10^3\}$
z_ℓ	Electrode contact impedance	$1 \times 10^{-4}\ \Omega \cdot m^2$
Injection parameters		
L	Number of electrodes	4
$\lvert E_\ell \rvert$	Electrode size	7 mm
E_{sp}	Distance between neighboring electrodes (side to side)	20 mm
E_{sh}	Shift of bottom electrodes to the right w.r.t. upper electrodes	$E_{sh} \in \{0, 6.75, 13.5\}$ mm

Since the forward problem is linear with respect to the injected currents, using more than three injection patterns would not increase the predictive power of the supervised learning methods. Also, since Kirchhoff's current law states that the sum of the currents flowing through all electrodes must be equal to zero, i.e.

$$\sum_{\ell=1}^{L} I_\ell = 0, \tag{2.14}$$

only up to $L-1$ voltages per injection can be linearly independent, and thus the last entry corresponding to the L^{th} electrode can be dropped, yielding

$$I = \begin{bmatrix} I_1 \\ I_2 \\ I_3 \end{bmatrix}. \tag{2.15}$$

Since the currents are applied at low frequencies, the distribution of the potential is governed by a Laplace equation. Because of the linearity of the latter, it is useful to write each injection pattern I as a linear combination of 3 base patterns:

$$I = a \begin{bmatrix} 1 \\ 0 \\ 0 \end{bmatrix} + b \begin{bmatrix} 0 \\ 1 \\ 0 \end{bmatrix} + c \begin{bmatrix} 0 \\ 0 \\ 1 \end{bmatrix}, \qquad \text{with} \quad a, b, c \in \mathbb{R}. \tag{2.16}$$

2.4.2 2D experiment with cavity

The set-up for the 2D cavity experiment is the same as that used for the 2D delamination experiment, except that the (zero-thickness) delamination is replaced by a rectangle of thickness 0.25 mm, whose boundaries are perfect insulators. Hence the electric current is prevented from flowing not only through the delamination, i.e. in the through thickness direction, but also horizontally around the delamination center. This aims at simulating the added resistance induced by fiber breakage in the delamination area. An example with such a cavity is shown in Figure 2.13.

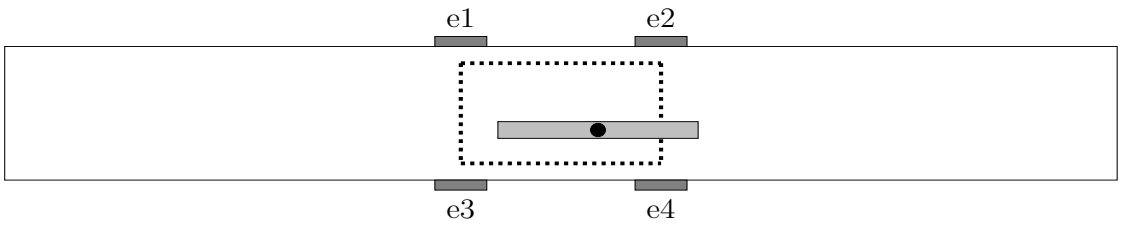

Figure 2.13 2D laminate with cavity. Generated cavities are always 0.25 mm thick.

CHAPTER 3 PARAMETER IDENTIFICATION USING SUPERVIZED LEARNING

The purpose of this chapter is to describe the methods that will be used to infer the presence of delamination in composite materials from voltages measured on the boundary. In machine learning, such a task is called *classification*, whose objective is in particular to specify which of k categories some input belongs to [22]. To solve this problem, the algorithm must produce a mapping $f : \mathcal{X} \mapsto \mathcal{Y}$ that assigns to each input vector $\mathbf{x} \in \mathcal{X}$, a category identified by numeric code $y = f(x) \in \mathcal{Y}$. The task in our problem consists of a binary classification problem, i.e. a classification problem with two classes: the positive class, labelled 1, which indicates the presence of a delamination, and the negative class, labelled 0, which is given to a sample when no delamination is present in the laminate.

An experience E denotes here the number of *training* samples, i.e. the observations the algorithm is trained with. The training dataset cannot be used to assess the performance of the machine learning model. For that purpose, a *test* dataset is held out during the training process, and then used to measure the performance P of the trained algorithm. This is because we are interested in how well the model *generalizes*, i.e. how well it performs on data the model has not yet seen nor been trained with.

In classification, the performance measure is often the model *accuracy*, which is defined as the proportion of inputs that are correctly labelled by the model. An equivalent measure is the error rate, namely the proportion of inputs that are incorrectly labelled by the model. The error rate is also referred to as the expected $0-1$ loss, because it assigns a loss of one to incorrect predictions and zero to correct predictions. In some binary classification problems, the two classes are not well balanced – one class might include most of the samples. In that case, we might be interested in the relative proportion of different types of errors rather than in overall accuracy. For example, in failure detection, a false positive (detecting a failure when it is not present) is valued differently from a false negative (not detecting a failure when it is present), for objective or subjective reasons.

In this chapter, we begin with describing how data must be preprocessed before it is fed to a learning algorithm. Preprocessing involves several steps:

1. Learning algorithms are designed to run in a specific framework and thus require the data to be structured accordingly. This process is known in the machine learning literature as data tidying [48];

2. While the forward problem is deterministic, uncertainties are inherent to real life measuring processes. These uncertainties are thus incorporated to the generated data in the form of noise;

3. When a large number features are involved, especially when dealing with three-dimensional data, training and prediction time can become a problem. In that situation, dimension reduction techniques may be needed to reduce the computational load.

Afterwards, we provide a brief but explicit description of the classification algorithms we will use:

- k-Nearest Neighbors;
- Random Forests;
- SVM with Radial Basis Function.

These three algorithms were chosen because they are non-parametric and constitute a representative sample of some of the most established algorithms in machine learning. Other learning algorithms could come to mind for solving this problem, but were rejected for different reasons. Linear Discriminant Analysis and Quadratic Discriminant Analysis [24] were discarded as they both assume that each class follows a Gaussian distribution. As classes are not linearly separable, using Logistic Regression [12] would necessitate to work within an enlarged data representation, which SVMs do more efficiently by using kernels to implicitly work within the enlarged representation. Artificial Neural Networks [22] are expensive in the training phase and require many choices to be made for their architecture.

3.1 Data preprocessing

This section is concerned with the actions that are performed on the data before it is fed to a learning algorithm.

3.1.1 Structure of the predictors matrix

In order to use supervised learning algorithms, the data is collected into a matrix where each column is a variable and each row an observation [48]. For the EIT problem, it means that, for each realization Θ_i of the delamination parameters, the computed electric potential data must be converted to a features vector x_i that contains the voltages measured at each current injection sites.

For a fixed injection I_k, we obtain potential U_i at the i-th electrode and thereby the voltages

$$V_1 = U_1 - U_2, \tag{3.1a}$$
$$V_2 = U_1 - U_3, \tag{3.1b}$$
$$V_3 = U_1 - U_4, \tag{3.1c}$$
$$V_4 = U_2 - U_3, \tag{3.1d}$$
$$V_5 = U_2 - U_4, \tag{3.1e}$$
$$V_6 = U_3 - U_4, \tag{3.1f}$$

where $U_1, \ldots, U_4$ are the electric potentials measured at the electrodes $1, \ldots, 4$, respectively. Since we use 4 electrodes, there are 3 degrees of freedom, so we will retain the first 3 voltages only. Hence the feature matrix takes the form

$$\mathbf{X}(\mathbf{\Theta}) = \begin{pmatrix} x_1^T \\ x_2^T \\ \vdots \\ x_N^T \end{pmatrix}, \qquad \text{where} \quad \mathbf{\Theta} = \begin{pmatrix} \Theta_1^T \\ \Theta_2^T \\ \vdots \\ \Theta_N^T \end{pmatrix} \qquad \text{and} \quad x_i = x(\Theta_i) = \begin{pmatrix} \mathbf{V}_1^{(i)} \\ \mathbf{V}_2^{(i)} \\ \mathbf{V}_3^{(i)} \end{pmatrix} \tag{3.2}$$

where for Θ_i, the i^{th} realization of Θ, and the k^{th} pattern injection (cf Section (2.4.1)), the vector $\mathbf{V}_k^{(i)} = (V_{k,1}^{(i)}, V_{k,2}^{(i)}, V_{k,3}^{(i)})$ contains the measured voltages. Each row x_i^T thus has $p = (4-1)^2 = 9$ entries.

3.1.2 Data splitting: Training and Test sets

The resulting data is split into two sets, namely the training set and the test set. The *training* set involves the data that the learning algorithms will use to learn about the structure of the data, i.e. to infer the delamination parameters from the voltage data. The *test* set is used to assess the performance of the algorithms, and in particular to evaluate how much we were able to learn from the training data.

The training observations indices are selected at random from the set of all the data indices, i.e. from one to N, the total number of rows in $\mathbf{X}$. We denote by $\mathbf{X}_{\text{train}}$ the $N_{\text{tr}} \times p$ matrix containing the p predictors of the N_{tr} training observations, and $\mathbf{X}_{\text{test}}$ the $N_{\text{ts}} \times p$ matrix containing the p predictors of the N_{ts} test observations, with $N_{\text{ts}} \leq N - N_{\text{tr}}$.

3.1.3 Modeling noise

The introduction of noise to the data aims at simulating measurement errors due to both the voltage measurement process and the intrinsic laminate properties. The first includes, for instance, small electrode displacements, contact resistance uncertainties at each of the probes, and differing injection intensities. The second concerns the uncertainty about the material conductivities due to material imperfection, i.e. the actual conductivities might differ slightly from the nominal values. It follows that the noise should be applied to the voltages. We directly use the measured voltages as predictors. Training data include many tiny delaminations, so the data span a small range of values around those of a pure undamaged laminate. In practice, these small variations on the training data are equivalent to noise. *Multiplicative* Gaussian noise is added to the data according to the formula

$$\mathbf{X}_{ij} \leftarrow \mathbf{X}_{ij}\,(1+\epsilon_{ij})\,, \qquad \text{with} \quad \epsilon_{ij} \sim \mathcal{N}(0,\nu^2) \tag{3.3}$$

where ν^2 denotes the noise variance. We choose *multiplicative* noise based on the fact that voltages are linearly related to material resistivity ($V = RI$), so that uncertainties about R give rise to proportional uncertainties about V (the injected currents I being held fixed). It also takes into account the limited number of significant digits of measurement instruments. The ϵ_{ij} are assumed to be identically and independently distributed. This assumption appears to be reasonable if we suppose that the uncertainties are associated to the path taken by the current and that the paths are essentially distinct. Also, as the tensions measured on an intact sample and on a sample with delamination are very close, see Figure 2.7, we assume that it is reasonable to reject negative values of $1+\epsilon_{ij}$.

Other researchers [44, 18] used voltages or resistance *changes* with respect to the undamaged laminate (or normalized changes) as predictors. However, they did not add noise to their data obtained from FEM computations.

3.1.4 Normalizing the predictors matrix

For some machine learning algorithms, especially in the case of instance-based methods such as kNN and SVM where the distance between training and query data points holds a primary importance, predictor scaling can have a significant influence on the prediction performance.

Often, when all the variables used for prediction are measured in the same units, we may choose not to scale them to have all the same standard deviation [27]. However, in the present case, the noise is multiplicative and hence proportional to each variable value, so information is not lost when scaling each column of $\mathbf{X}$ in order to have a variance equal to unity.

When scaling is required, each predictor is transformed using the formula

$$V_j^k \leftarrow \frac{(V_j^k - \overline{V}_{j,\mathrm{tr}}^k)}{\mathrm{sd}(V_{j,\mathrm{tr}}^k)}, \quad \text{where} \quad \overline{V}_{j,\mathrm{tr}}^k = \frac{1}{N_{\mathrm{tr}}} \sum_{i=1}^{N_{\mathrm{tr}}} V_j^{k(i)} \tag{3.4}$$

$$\text{and} \quad \mathrm{sd}(V_{j,\mathrm{tr}}^k) = \sqrt{\frac{1}{N_{\mathrm{tr}} - 1} \sum_{i=1}^{N_{\mathrm{tr}}} (V_j^{k(i)} - \overline{V}_{j,\mathrm{tr}}^k)^2}. \tag{3.5}$$

Note that the mean and standard deviation are always taken on the training data, whether the data that are being scaled are in the training set or in the test set. Scaling the predictors has no impact on the performance of tree-based methods. It should be noted that, if instead of being multiplicative, the noise had a log-normal distribution, using the logarithm of the predictors would make more sense than scaling them.

3.1.5 Dimensionality reduction

As we focus on mainstream methods rather than trying to optimize each algorithm for the EIT application, we did not consider dimension reduction. Instead, we simplified the case study as much as possible, keeping only four electrodes. Some researchers sought to minimize the cost of the analysis by reducing the number of measurements used to solve the inverse problem. Escalona-Galvis et al. [17] used the Effective Independence measure, see e.g. Kammer [28], to select an optimal subset of resistance measurements by eliminating redundant electrode pairs. Another approach is to reduce the dimensionality of the data after collecting the voltage (or resistance) measurements. One common way to do this is to retain only the top principal components. However, Principal Component Analysis (PCA) only captures linear dependencies between predictors. Auto encoders have the advantage of being capable of capturing non linear dependencies between predictors [25].

3.2 Supervised learning methods for inference on the presence of delamination

In this section, we address the problem of binary classification. We begin by creating a new target variable Y, taking the value 1 when the delamination size ρ is greater than a given threshold a, and the value 0 otherwise. In other words, for a given observation x_i:

$$y_i = \begin{cases} 1 & \text{if } \rho_i \geq a; \\ 0 & \text{if } \rho_i < a. \end{cases} \tag{3.6}$$

We thus create the vector $\mathbf{y_{tr}}$ of the y_i's, $i = 1, \ldots, N_{\mathrm{tr}}$, associated with the training set

and the vector $\mathbf{y_{ts}}$ of the y_i's, $i = 1, \ldots, N_{\text{ts}}$, associated with the test set. For a given test observation x_0, the goal is to estimate the conditional probabilities $P(Y = 1|\, x_0)$ and $P(Y = 0|\, x_0)$. The predicted class $\hat{y}_0$ is generally given as the one maximizing the likelihood, hence

$$\hat{y}_0 = \underset{y}{\operatorname{argmax}}\, P(Y = y \,|\, x_0). \tag{3.7}$$

In practice, the value of a would be given by experts who determined when the composite needs attention. We chose a to be the expected width of the delamination so as to obtain well-balanced classes. Furthermore, the classification problem would have been as difficult for any value of a in a reasonable range around the mean because the variations in the signal are very weak with respect to the delamination width. For these reasons, it was not useful to search for an optimal threshold a.

We now proceed to describe the machine learning algorithms that we shall compare in this study.

3.2.1 k-Nearest-Neighbors

The k-NN method is an example of instance-based learning: rather than fitting a model, its predictions are based on the labels of the k points in the training set whose features are the closest to the query point's features. This method is also described as "lazy", since no generalization about the data structure is made until a new observation needs to be labelled [24]. More precisely, given a positive integer k and a test observation x_0, the kNN classifier first identifies the k points in the training data that are the closest to x_0, represented by $\mathcal{N}_0$. It then estimates the conditional probability for class j as the fraction of points in $\mathcal{N}_0$ whose response values equal j [27]. In other words, the conditional probability for class j at x_0 is estimated by

$$P(Y = j|X = x_0) = \frac{1}{k} \sum_{i \in \mathcal{N}_0} I(y_i = j), \tag{3.8}$$

where $I(y_i = j)$ is the indicator function taking value one when $y_i = j$ and zero otherwise. The test observation x_0 is then classified to the class with the largest probability. Since predictions rely entirely on the distance measure between test or training observations, this method is highly sensitive to variables preprocessing, including rescaling and features selection. In our case, the distance between the query point and the points in the training set is the Euclidian distance on features previously scaled to all have variance one (since the noise is Gaussian multiplicative). If the noise followed a log-normal distribution, the Euclidian distance on the predictors logarithm would be more appropriate.

The choice of the hyperparameter k, also called tuning parameter, is a model selection problem. In statistics, common techniques for assessing the adequacy of a model include the Akaïke Information Criterion (AIC) [1] and the Bayesian Information Criterion (BIC) [39], which use a penalty term for the number of parameters in the model. However, those estimates require a precise evaluation of the number of model parameters, which is hard for methods such as kNN. Hence, an estimate $\hat{k}$ of k^* (the true optimal k) is chosen based on an estimate of prediction error, computed using cross-validation. The latter is described in section 3.3.2.

3.2.2 An estimate of the Bayes rate lower bound

The Bayes error is the lowest possible error rate for a given classification problem [46]. It is the error associated with the Bayes classifier, namely the classifier that assumes knowledge of the true class probabilities at all points $x \in \mathcal{X}$. It is non-zero if the classification labels are not deterministic, i.e. there is a non-zero probability of a given instance belonging to more than one class. According to Tumer and Ghosh [46], "such information is helpful in determining whether it is worthwhile to try a different classifier, or a different set of parameters with the chosen classifier with the hope of getting better classification rates". The Bayes error is given by

$$E_{Bayes} = 1 - \sum_{i=1}^{K} \int_{\mathcal{K}_i} p(k_i|x)dx, \tag{3.9}$$

where $p(k_i|x)$ is the posterior for class k_i at point x, and $\mathcal{K}_i$ is the domain where k_i is the dominant class, i.e. the class with the largest posterior. However, the $\mathcal{K}_i$ and $p(k_i|x)$ are not known, so an estimate is needed.

We estimate a lower bound on the Bayes rate using the one-nearest-neighbor rule. Cover and Hart [11] showed that asymptotically

$$E_{Bayes} \leq E_{1\text{NN}} \leq 2E_{Bayes}(1 - E_{Bayes}) \leq \frac{1}{2} \tag{3.10}$$

where $E_{1\text{NN}}$ denotes the classification error obtained if using the k-nearest-neighbor with $k = 1$ to make predictions on test data. Hence

$$\begin{aligned} & E_{Bayes}^2 - E_{Bayes} + \frac{E_{1\text{NN}}}{2} \leq 0 \\ \iff & \frac{1 - \sqrt{1 - 2E_{1\text{NN}}}}{2} \leq E_{Bayes} \leq \frac{1 + \sqrt{1 - 2E_{1\text{NN}}}}{2}. \end{aligned}$$

The upper bound is useless since we already know that $E_{Bayes} \leq \frac{1}{2}$, but we plot the lower bound together with the error rates of the machine learning algorithms in Chapter 4 to get an idea of how close the latter are to optimality.

3.2.3 Random forests

A random forest is defined by Breiman [9] as "classifier consisting of a collection of tree-structured classifiers $\{h(x, \Theta_k), k = 1, \ldots\}$ where the Θ_k are independent and identically distributed random vectors and each tree casts a unit vote for the most popular class at input x". We describe here its most popular form, which consists in applying the ensemble method known as "Bagging" (Bootstrap aggregating) to fully grown (i.e. not pruned) trees, while keeping the latter as independent as possible from each other by using only a subset of the features at each step of the tree-growing process. We begin with a description of the classification tree algorithm and the bagging ensemble method, before explaining the improvement brought by random forests over simple bagged trees.

The tree-structured classifier

Classification and Regression Trees (CART) were first proposed by Breiman [7]. Whether they are used for classification or regression, tree-based methods consist in partitioning the feature space into a set of blocks, and then fitting a simple model in each one. Contrary to instance-based methods, they have the advantage of being immune to scaling, and are particularly popular in data analysis because of their simplicity of interpretation [24].

For a number N_{tr} of observations, our data consists of p inputs $x_i = (x_{i1}, x_{i2}, \ldots, x_{ip})$ and a response y_i, $i = 1, \ldots, N_{\text{tr}}$, for each of N_{tr} observations. Suppose that we have a partition of $\mathcal{X} = \mathbb{R}^p$ into M regions $R_1, R_2, \ldots, R_M$.

For a node m representing a region R_m with N_m observations, let

$$\hat{p}_{mk} = \frac{1}{N_m} \sum_{x_i \in R_m} I(y_i = k) \tag{3.11}$$

be the proportion of class k observations in node m. We classify the observations in node m to class $k(m) = \text{argmax}_k \hat{p}_{mk}$, the class that collects the most votes in node m.

A greedy, top-down recursive partitioning algorithm is used to find the partition. Starting with all the data, consider a splitting variable j and split point s, and define the pair of half-planes

$$R_1(j, s) = \{X | X_j \leq s\} \quad \text{and} \quad R_2(j, s) = \{X | X_j > s\} \tag{3.12}$$

Choosing the Gini index [24] as measure of node impurity, we seek the splitting variable j and split point s that solve

$$\min_{j,s} \hat{p}_{11}\hat{p}_{12} + \hat{p}_{21}\hat{p}_{22}, \tag{3.13}$$

which can also be written

$$\min_{j,s} \hat{p}_{11}(1 - \hat{p}_{11}) + \hat{p}_{21}(1 - \hat{p}_{21}). \tag{3.14}$$

Other measures of node impurity exist, like the misclassification error $1-\hat{p}_{mk}$ and the entropy $-\sum_{k=1}^{K} \hat{p}_{mk} \log \hat{p}_{mk}$.

As opposed to misclassification error, entropy and Gini index are differentiable, and thus more suitable for numerical optimization. They are also more sensitive to changes in probability than the misclassification rate. Experimentally, entropy and Gini index yield similar results. Here, the Gini index is used as the splitting criterion.

Having found the best split, the splitting process is repeated on each resulting region. When growing a single (non-bagged) tree, the preferred strategy is generally to grow a large tree T_0, stopping the splitting process only when some minimum node size is reached, and then "pruning" the tree, i.e. choosing the optimal tree size using cross-validation. However, this last step is not applied when growing a forest, since we want each tree to have a low bias.

Bootstrap

The bootstrap method consists of randomly drawing datasets with replacement from the training data, each sample being of the same size N_{tr} as that of the training dataset $\mathcal{T}$. This is done B times, producing B bootstrap datasets, the model being fit on each of the bootstrap datasets.

Let the empirical distribution function $\hat{F}$ be the distribution that assigns a probability mass $\omega = \frac{1}{N_{\text{tr}}}$ on x_i, $i = 1, 2, \ldots N_{\text{tr}}$. It can be shown that $\hat{F}$ is the *non parametric maximum likelihood estimate* of the true underlying population F [15]. Since drawing with replacement from the training set $\mathcal{T}$ is the same as drawing samples from $\hat{F}$, the non parametric bootstrap can be seen as maximum non parametric likelihood inference.

The method we just described is called the *non-parametric* bootstrap, because it uses the raw data and not a specific parametric model to generate new datasets [24].

Bagging

Bagging [8], short for bootstrap aggregating, makes use of the bootstrap to reduce the variance of an estimated prediction. Each derivative "bootstrapped" data set is used to construct a new model and the models are gathered together into an ensemble.

Bagging averages the predictions produced by the models fit on a collection of bootstrap samples. The bagging prediction $\hat{f}(x)$ is thus given by

$$\hat{f}_{bag}(x) = \frac{1}{N_B} \sum_{b=1}^{N_B} \hat{f}^b(x) \tag{3.15}$$

where N_B is the number of bootstrap samples. In classification, to make a prediction, all models in the ensemble are polled and their results are averaged.

Since each tree generated in bagging is identically distributed (i.d.), the expectation (the prediction) of an average of N_B such trees is the same as the expectation of any one of them, i.e. the bias of bagged trees is the same as that of the individual trees. The improvement is left to variance reduction. Thus bagging works especially well for algorithms that have high-variance and low bias, such as fully-grown trees. The latter have relatively low bias if grown sufficiently deep, but suffer from high variance.

To further improve variance reduction, random forests add another parameter to bagging trees.

Random forests

Random forests modify bagging by decorrelating the trees through random selection of the input variables during the tree-growing process. When growing a tree on a bootstrapped dataset, the following rule is observed:

Before each split, select $m_{try} \leq p$ of the input variables at random as candidates for splitting.

After N_B such trees $\{T(x; \Theta_b)\}_1^{N_B}$ are grown, the random forest (regression) predictor is

$$\hat{f}_{\mathrm{rf}}^{N_B}(x) = \frac{1}{N_B} \sum_{b=1}^{N_B} T(x; \Theta_b). \tag{3.16}$$

where Θ_b characterizes the bth random forest tree in terms of split variables, cutpoints at each node, and terminal-node values.

The number N_B of trees grown on individual bootstrap samples does not need to be tuned. This is due to the fact that a random forest cannot overfit the data: since the model is

averaged over all the trees, the variance can only decrease. One must just make sure that N_B is large enough for convergence of the error rate. Random forests always converge [9].

The following parameters remain to be tuned:

- m_{try}, the number of variables to be tried at each split;
- the node size, i.e. the minimum number of observations contained in a terminal node.

Hastie et al. [24] report that, from experience, "using full-grown trees seldom costs much, and results in one less tuning parameter". This matches our experience with the data at hand: the optimal tuning parameter combination almost always has a node size equal to one. This can be explained by the fact that a fully grown tree has less bias than a shallow tree. Thus we can set the node size to one and tune only m_{try}. This results in a much reduced computational cost.

Being immune to scaling might not be such an advantage the random forest have over instance-based methods when the noise distribution is known, since the latter is used to decide whether the variables should be scaled or not. However, in situations where one is unsure if the noise should be additive or multiplicative (or a mix of both), it can turn out to be a decisive property. The randomForest package of Liaw et al. [31] provides an R interface to the Fortran programs by Breiman and Cutler.

3.2.4 Support Vector Machines

The modern version of the SVM algorithm first appeared in Cortes and Vapnik [10]. The SVM algorithm separates classes by constructing linear boundaries in a transformed version of the feature space. Our training data consists of N_{tr} pairs $(x_1, y_1), (x_2, y_2), \ldots, (x_{N_{\text{tr}}}, y_{N_{\text{tr}}})$, with $x_i \in \mathbb{R}^p$ and $y_i \in \{-1, 1\}$ such that:

$$y_i = \begin{cases} 1 & \text{if } \rho_i \geq a; \\ -1 & \text{if } \rho_i < a. \end{cases} \tag{3.17}$$

We follow the description found in Hastie et al. [24]. A hyperplane in $\mathbb{R}^p$ can be defined by

$$\{x \in \mathbb{R}^p : f(x) = x^T\beta + \beta_0 = 0\} \tag{3.18}$$

where β is a unit vector, i.e. $\|\beta\| = 1$. The function $f(x)$ gives the signed distance from point x to the hyperplane $x^T\beta + \beta_0 = 0$ and the sign can be used as a classification rule. When

classes are linearly separable, we can find a function $f(x) = x^T\beta + \beta_0$ with $y_i f(x_i) > 0, \forall i$. To maximize the margin $M \in \mathbb{R}$ between the training points of both classes, define the optimization problem

$$\begin{aligned} \max_{\beta,\beta_0,||\beta||=1} \quad & M \\ \text{subject to} \quad & y_i(x_i^T\beta + \beta_0) \geq M,\ i = 1, \ldots, N_{\text{tr}}, \end{aligned} \tag{3.19}$$

which can be recast as:

$$\begin{aligned} \min_{\beta,\beta_0} \quad & \|\beta\| \\ \text{subject to} \quad & y_i(x_i^T\beta + \beta_0) \geq 1,\ i = 1, \ldots, N_{\text{tr}}. \end{aligned} \tag{3.20}$$

Minimizing $\|\beta\|$ is equivalent to minimizing $\|\beta\|^2$, hence 3.20 is equivalent to the convex optimization problem

$$\begin{aligned} \min_{\beta,\beta_0} \quad & \frac{1}{2}\|\beta\|^2 \\ \text{subject to} \quad & y_i(x_i^T\beta + \beta_0) \geq 1,\ i = 1, \ldots, N_{\text{tr}}. \end{aligned} \tag{3.21}$$

To deal with classes overlapping, we can define the slack variables $\eta_i,\ i = 1, \ldots, N_{\text{tr}}$ and rewrite (3.21) as follows:

$$\begin{aligned} \min_{\beta,\beta_0} \quad & \frac{1}{2}\|\beta\|^2 + C\sum_{i=1}^{N_{\text{tr}}} \eta_i \\ \text{subject to} \quad & y_i(x_i^T\beta + \beta_0) \geq 1 - \eta_i, \\ & \eta_i \geq 0,\ \forall i, \end{aligned} \tag{3.22}$$

where the parameter C controls the trade-off between the slack variable penalty and the size of the margin. To find the optimal β, β_0 we can minimize the corresponding Lagrange primal function

$$L_P(\beta, \beta_0, \eta) = \frac{1}{2}\|\beta\|^2 + C\sum_{i=1}^{N_{\text{tr}}} \eta_i - \sum_{i=1}^{N_{\text{tr}}} \alpha_i[y_i(x_i^T\beta + \beta_0) - (1 - \eta_i)] - \sum_{i=1}^{N_{\text{tr}}} \mu_i\eta_i. \tag{3.23}$$

Differentiating with respect to β, β_0, and η_i, and setting the derivatives to zero, we get

$$\frac{\partial L_P}{\partial \beta} = 0 \quad \Rightarrow \quad \beta = \sum_{i=1}^{N_{\text{tr}}} \alpha_i y_i x_i, \tag{3.24a}$$

$$\frac{\partial L_P}{\partial \beta_0} = 0 \quad \Rightarrow \quad \sum_{i=1}^{N_{\text{tr}}} \alpha_i y_i = 0, \tag{3.24b}$$

$$\frac{\partial L_P}{\partial \eta_i} = 0 \quad \Rightarrow \quad C = \alpha_i + \mu_i, \ \forall i, \tag{3.24c}$$

together with positivity constraints $\alpha_i, \mu_i, \eta_i \geq 0$. By substituting these equations into (3.23), we obtain the Lagrange dual objective function

$$L_D = \sum_{i=1}^{N_{\text{tr}}} \alpha_i - \frac{1}{2} \sum_{i=1}^{N_{\text{tr}}} \sum_{j=1}^{N_{\text{tr}}} \alpha_i \alpha_j y_i y_j x_i x_j, \tag{3.25}$$

which we maximize subject to $0 \leq \alpha_i \leq C$ and $\sum_{i=1}^{N_{\text{tr}}} \eta_i y_i = 0$. In addition, the Karush-Kuhn-Tucker (KKT) conditions include the constraints

$$\alpha_i [y_i (x_I^T \beta + \beta_0) - (1 - \eta_i)] = 0, \tag{3.26a}$$

$$\mu_i \eta_i = 0, \tag{3.26b}$$

$$y_i (x_i^T \beta + \beta_0) - (1 - \eta_i) \geq 0, \quad \forall i = 1, \ldots, N_{\text{tr}}. \tag{3.26c}$$

Together, equations (3.24)-(3.26) uniquely characterize the solution to the primal and dual problem. Until now, the method is limited to linear boundaries. To extend it to more complex boundary shapes, one can define enlarged feature vectors $h(x)$. From (3.24a) we see that the solution function $f(x)$ can be written

$$f(x) = h(x)^T \beta + \beta_0 = h(x)^T \left(\sum_{i=1}^{N_{\text{tr}}} \alpha_i y_i h(x_i) \right) + \beta_0 = \sum_{i=1}^{N_{\text{tr}}} \alpha_i y_i \, h(x)^T h(x_i) + \beta_0. \tag{3.27}$$

From (3.25) and (3.27) we see that $h(x)$ is only involved through inner products. Hence we do not need to specify $h(x)$ but only the kernel function

$$K(x, x') = h(x) \cdot h(x'). \tag{3.28}$$

In this study, we use the radial basis function kernel

$$K(x, x') = \exp(-\gamma \|x - x'\|^2). \tag{3.29}$$

The corresponding feature vector has an infinite number of dimensions but does not need to be specified. The γ parameter defines how far the influence of a single training sample selected by the model as support vector reaches, while the C parameter trades off correct classification of training examples against maximization of the decision function's margin. The choice of these parameters is discussed in the next section. We use the R library described in Meyer and Wien [32].

3.3 Model selection

Model parameters are learnt directly from data, while hyper-parameters are used in the model parameter estimation process, and must be tuned using heuristics. The parameter γ in the SVM radial basis kernel (cf (3.29)), the number of neighbors k in the k-nearest neighbors method and the number m_{try} of variables among which to chose a split point during the construction of each random forest tree, are examples of such hyper-parameters. The tuning of these hyper-parameters amounts to a model selection problem. In this study, we will use cross-validation, a popular method that allows us to use the training set to perform both training and model selection, to select them.

This section begins with some comments about the metric used in this study. We then give a brief description of cross-validation and provide a few details of its implementation for the learning algorithms that are used in this work.

3.3.1 Performance metric

The performance of a classification algorithm can be completely summarized by a confusion matrix. The confusion matrix is a $K \times K$ table collecting in each cell (i, j) the number of observations that belong to class j that were predicted to belong to class i, for each $i, j = 1, \ldots, K$. Since we are doing binary classification, the confusion matrix here is 2×2.

Many different performance measures can be computed from the confusion matrix, the choice of the measure depending on the data at hand and on the goal of the data analysis. In this study, we choose to report the error rate, defined as the ratio of misclassified test samples over the total number of test samples. We sometimes also report false positives and false negatives separately in order to provide a thorough analysis of these different error types.

Table 3.1 Confusion matrix for binary classification

	Predicted Positive	*Predicted Negative*
Real Positive	True Positive (TP)	False Negative (FN)
Real Negative	False Positive (FP)	True Negative (TN)

3.3.2 Cross-validation

Cross-validation is used to estimate the test error of a model in order to perform model selection. While some less expensive model selection procedures (C_p and BIC statistics) are available, they all require the knowledge of the number of parameter. Cross-validation does not require the latter to be known, and therefore is more appropriate in complicated settings [15]. While using separate training and validation sets is better when we have plenty of data, cross-validation is preferred in situations where data are rare or expensive to collect, as in our case.

Cross-validation consists of using part of the training data to fit the model, and the rest to test it. In V-fold cross-validation, we partition the training dataset

$$\mathcal{T} = \{(x_1, y_1), (x_2, y_2), \dots (x_{N_{\text{tr}}}, y_{N_{\text{tr}}})\}$$

randomly into V equally sized non-overlapping subsets indexed by $v \in \{1, \dots, V\}$. For the v^{th} part, we fit the model to the other $V-1$ parts of the data, and calculate the prediction error of the fitted model when predicting the v^{th} part of the data. We do this for $v = 1, 2, \dots, V$ and combine the estimates of prediction error: the cross-validation estimator of the prediction error is defined as the average of the prediction errors obtained on each fold.

Let $\kappa : \{1, \dots, N_{\text{tr}}\} \mapsto \{1, \dots, V\}$ be an indexing function that indicates the partition to which the observations are allocated by the randomization. Denote by $\hat{f}^{-v}(x)$ the fitted function, computed with the v^{th} part of the data removed. Then the cross-validation estimate of prediction error is

$$\text{err}_{CV}(\hat{f}) = \frac{1}{N_{\text{tr}}} \sum_{i=1}^{N_{\text{tr}}} L(y_i, \hat{f}^{-\kappa(i)}(x_i)), \tag{3.30}$$

where $L(y_i, \hat{f}^{-\kappa(i)}(x_i))$ is the loss incurred by estimating y_i with $\hat{f}^{-\kappa(i)}(x_i)$. Given a set of models $f(x, \alpha)$ indexed by a tuning parameter α, denote by $\hat{f}^{-v}(x, \alpha)$ the α^{th} model fit with the v^{th} part of the data removed. Then for this set of models we define

$$\text{err}_{CV}(\hat{f}, \alpha) = \frac{1}{N_{\text{tr}}} \sum_{i=1}^{N_{\text{tr}}} L(y_i, \hat{f}^{-\kappa(i)}(x_i, \alpha)). \tag{3.31}$$

The function $\text{err}_{CV}(\hat{f}, \alpha)$ provides an estimate of the test error curve, and we find the tuning parameter $\hat{\alpha}$ that minimizes it. The final chosen model is $f(x, \hat{\alpha})$, which we then fit to all the training data.

3.3.3 Application of cross-validation to the machine learning algorithms

We now give precisions concerning the implementation of cross-validation for the algorithms used in this study.

k-NN For the k-NN method, the tuning parameter α is the number of neighbors of the test observation to be taken into account in the prediction. Kohavi [29] recommends using stratified 10-fold CV. In our case, we have two well-balanced classes with hundreds of samples per class, so we choose $V = 10$ without stratification.

The loss function used is the misclassification rate, i.e.

$$L(y, \hat{f}(x, \alpha)) = I(y \neq \hat{f}(x, \alpha)) = \begin{cases} 1 & \text{if } \hat{f}(x, \alpha) \neq y, \\ 0 & \text{otherwise.} \end{cases} \tag{3.32}$$

Substituting (3.32) for $\hat{f}^{-\kappa(i)}(x_i, \alpha)$ in (3.31), we obtain the cross-validation error estimate for the k-nearest neighbors method:

$$\text{err}_{CV}(\hat{f}, k) = \frac{1}{N_{\text{tr}}} \sum_{i=1}^{N_{\text{tr}}} I(y_i \neq \hat{f}^{-\kappa(i)}(x_i, k)). \tag{3.33}$$

The value of k that yields the smallest $\text{err}_{CV}(\hat{f}, k)$ is then chosen to make predictions on the test set from the whole training set. In our case, k is an odd natural number chosen between 1 and 41, as preliminary results showed k was always under 41.

Random Forests A grid search is conducted over the parameter m_{try}, using the Out-Of-Bag (OOB) error estimate. Recall that bootstrap samples are each generated by drawing N_{tr} times with replacement from the N_{tr} training observations. Thus each observation has probability

$$\left(1 - \frac{1}{N_{\text{tr}}}\right)^{N_{\text{tr}}} = e^{-1} \approx 0.368$$

of not being included in a given bootstrap sample. The training data that are not included in a given bootstrap sample are called OOB observations. The OOB error is computed by averaging, for each observation $z_i = (x_i, y_i)$, over only those trees grown on bootstrap

samples which do not contain z_i. The value of m_{try} that yields the smallest OOB error is then used to fit the final model. The OOB error can also be used to assess when training can be terminated. No more trees need to be constructed once the OOB error stabilizes. As preliminary results showed the error stabilizes after about 500 trees are grown, we choose to grow a conservative 1,000 trees. m_{try} is chosen between 1 and 9 (the total number of predictors in our study).

Support Vector Machines As with the k-nearest-neighbor method, we use 10-fold cross-validation to select the optimal hyper-parameters of the SVM method. However, this time, two hyper-parameters must be selected, i.e. the kernel width γ and the cost C. A grid-search is performed: we look for the best $\{\gamma, C\}$ in $\{0.005, 0.05, 0.5\} \times \{1, 10, 100, 1000\}$.

CHAPTER 4 NUMERICAL RESULTS

In this chapter, we present the numerical results. We consider two cases: first, we use a subset of our data containing only delaminations that are either clearly large or small, and therefore easy to classify, to check if the results match our intuition. Secondly, using the full dataset, we attempt to give answers to the questions raised in the introduction:

- Is there an algorithm that stands out as the most appropriate tool for solving the inverse problem?
- How much impact has noise on the prediction performance?
- How many training samples are needed to achieve a near-optimal prediction performance?
- Which electrode setting provides the most informative data?
- How much harder is delamination detection in comparison to detecting a cavity representing the added resistance change due to fiber breakage?

The results provide insights about the complex relationship between noise, anisotropy and geometry, which motivates us to recommend further research on precise aspects of this subject.

4.1 Preliminary results with well separated classes

The objective in this section is to verify that the code was correctly implemented by computing the prediction error of all algorithms on subsets of data with well-separated classes. For that purpose, we only keep the samples that have a delamination radius ρ that is either at least three millimeters smaller than the threshold $a = 6.75$ mm, i.e. $\rho \leq 3.75$ mm, or greater, i.e. $\rho \geq 9.75$ mm. The latter are considered to be damaged, while the first are considered in good state. Data samples with $3.75 \leq \rho \leq 9.75$ mm are not used in this section but will be considered in Section 4.2.1. The motivation is that removing the ambiguous samples will shed light on some trends that might otherwise be harder to observe and lead to clearer results to interpret.

4.1.1 Prediction performance on test data

We begin by plotting the error rates of each algorithm against the noise's standard deviation. Results are shown in Figure 4.1. The algorithms are trained on 400 samples and produce predictions on 100 test samples, 10 times. Each point corresponds to the average of the 10 error rates obtained, and the error bars are the standard deviations computed over those 10 error rates. Each computation involves each of the steps described in Chapter 3, from the addition of noise to cross-validation.

As expected, the error rates are equal or very close to perfect when data are noiseless, except when the anisotropy is low, i.e. $\lambda = 1$ or $\lambda = 10$, and bottom electrodes are not shifted to the right. Another observation is that the error rate is not a monotonic function of the conductivity ratio λ. While it has been said on multiple occasions that the main difficulty in delamination detection in CFRP is the high electrical anisotropy, our results seem to show that the detection of damage is easier with a moderately high anisotropy, i.e. $\lambda = 100$, when noise intensity is kept under a few percent.

When $\lambda = 1000$, the curves in Figure 4.1 have a parabolic profile for low values of the noise. The prediction performance is ideal on deterministic data and remains good when $\nu = 1\%$, but then worsens quickly. Since we are in the context of binary classification, as $\nu^2 \to \infty$, the average error rate cannot be greater than $1 - p_{k^*}$, where p_{k^*} is the proportion of k^*, the most represented class in the data, and the derivative of the error rate with respect to ν must vanish. Thus the error rate slowly starts to stabilize after an inflexion point is attained when $\nu \sim 2.5\%$. The same behavior is seen for $\lambda = 100$, except that this time the inflexion point is attained much later, when $\nu \sim 8\%$. However, for $\lambda = 1$ or 10 the error rate linearly increases in the range visible in the graph, i.e. for $\nu < 10\%$.

SVM and random forests yield similar performance overall. k-NN prediction errors are generally a little greater. The Bayes rate estimate is only slightly smaller than SVM and random forests prediction errors and often hardly distinguishable from the latter until a gap appears after the noise standard deviation attains a few percent. Overall, these observations indicate that using other machine learning algorithms would not lead to significantly more accurate predictions.

4.1.2 Location of misclassified samples

To gain more insights about the predictions errors, we display the positions of false negatives and false positives in Figure 4.2. In this graph, the electrode shift E_{sh} is fixed at zero; the solid horizontal black lines at each corner signal the electrode positions. Note that vertical

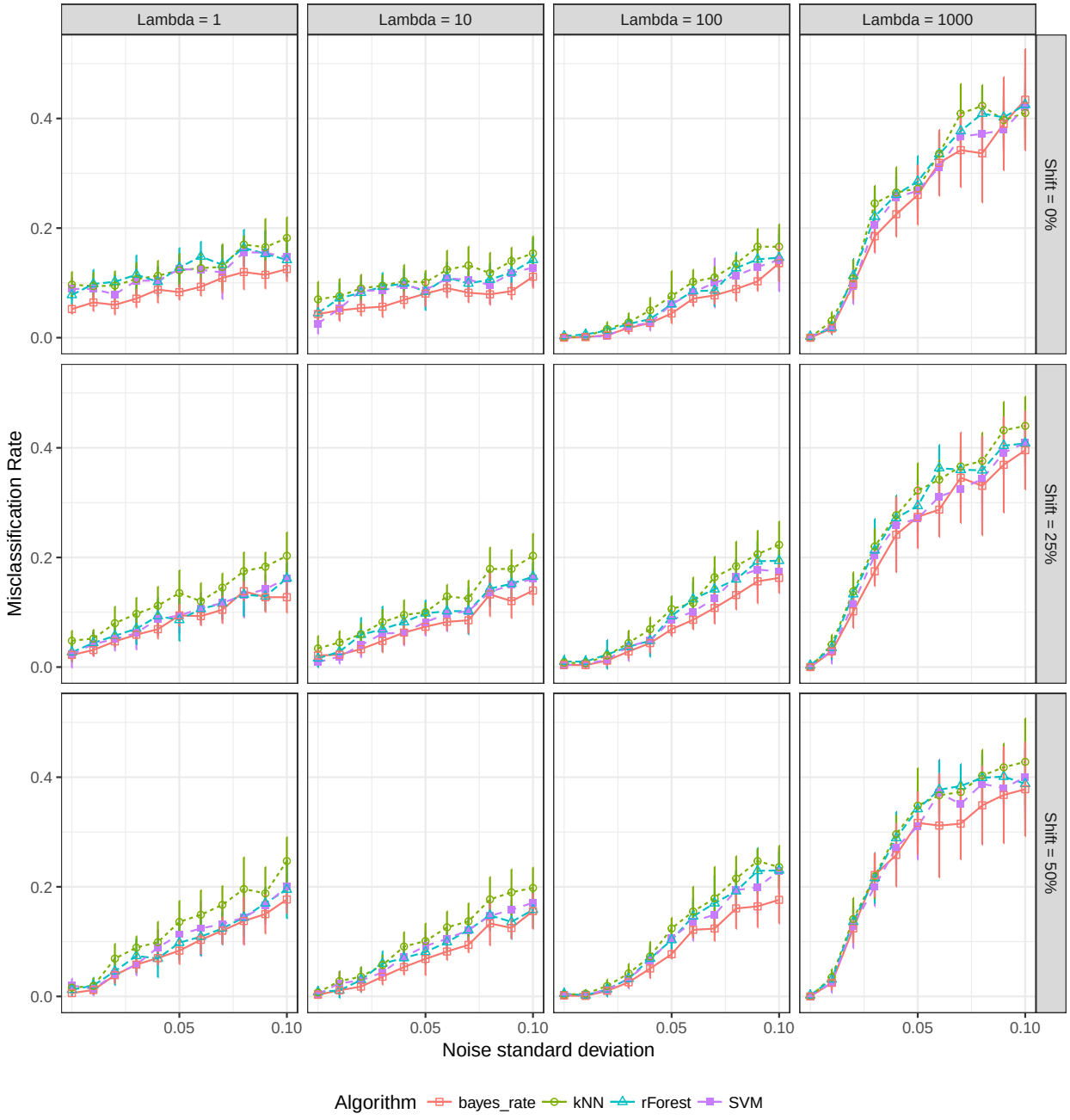

Figure 4.1 Misclassification rate as a function of the noise standard deviation. 400 training data, 100 test data, repeated 10 times, in the case of well-separated 2D delamination sizes. Electrode shift values are shown on the right.

distances are exaggerated: the geometry of the samples under study is still the one displayed in Figure 2.10, but we only show the part of the geometry that is between the electrode in order to obtain a better resolution.

We first notice is that for $\lambda = 1$ and ν close to zero, the locations of the two different error types are well separated. On one hand, all the false positives (insignificant damage that were predicted positive) are located close to the electrodes. As these delaminations stand right in the path between electrodes, they force the current to take a path that is significantly longer than the one it would follow without the presence of a (small) delamination. Furthermore, the two closest electrodes are the ones that are most solicited by this delamination, and hence are likely to lead to more sensitive measurements. Effectively, this leads to strong signals from what should be negligibly small delaminations being detected between the two closest electrodes.

On the other hand, false negatives (harmful delamination that went undetected) are all found in the center, midway between left and right electrodes and thus far away from both. The delaminations would cause increases in the voltage drops between the two most separated electrodes, and hence would correspond to the least sensitive positions for delamination detection. Although the larger delaminations are misclassified when they are in the middle, this seems reasonable since they correspond to larger voltage drops (longer paths and more path options) and thereby least available discrimination of the sources of these voltage drops. However, the separation of these two error types becomes less clear as λ increases. When $\lambda = 1000$ and $\nu > 3\%$, the locations of both error types seem uniformly distributed. While Figure 4.2 only shows damage location for $E_{sh} = 0$, we observe the same behavior for $E_{sh} = 25\%$ and $E_{sh} = 25\%$.

Another general trend we notice is that as ν increases, a left-right bias seems to appear: false positives occurs more frequently on the left side, while false negatives are more prominent on the right side. We attempt to explain this observation in the next section.

4.1.3 Sources of left-right bias

To explain the left-right bias observed in Figure 4.2, we review choices we previously made about features selection and noise distribution. We noticed that when $\sigma > 0$ the majority of false negatives occur for delaminations located on the right part of the composite, while false positives are more likely to happen on the left side. One source of bias is that we did not use all possible electrode pairs for current injection. We only used three of the six possible pairs: the pairs (1,2), (1,3), and (1,4). Since our measurements are more sensitive to damage located on the path followed by the current between each of these electrode pairs, we are more

Figure 4.2 Location of test delaminations misclassified by SVM algorithm, with Shift=0%, ν from 0 to 0.05, 400 training data, 100 test data, repeated 10 times. Corresponding noise intensities ν are shown on the right.

susceptible to detect delamination between electrodes 1 and 3 than between electrodes 2 and 4. It is also worth mentioning that, as the paths taken by the electrical current depend on λ, so does the correlation between voltage measurements, making the problem more complex.

Another cause for the bias is that $V_5 = U_2 - U_4$ does not appear explicitly among the predictors. Instead it is measured indirectly through voltages $V_1 = U_1 - U_2$ and $V_3 = U_1 - U_4$, that is

$$V_5 = U_2 - U_4 = (U_1 - U_4) + (U_2 - U_1) = V_3 - V_1, \tag{4.1}$$

hence the variance of V_5 is equal to the sum of the variance of V_1 and V_3. The same remark can be made about voltages V_4 and V_6, but the data does not clearly show a bias in those cases.

Recall that in equation (3.3), we supposed that the noise terms ϵ_{ij} affecting each voltage feature were all pairwise independent. In reality, paths taken by the current to go from electrode 1 to electrodes 2, 3, and 4 overlap in the region surrounding electrode 1, and hence voltages V_1, V_2, and V_3 are correlated. Taking these (positive) correlations into account would reduce the variance of V_5, since

$$\mathrm{Var}[A + B] = \mathrm{Var}[A] + \mathrm{Var}[B] + 2 \times \mathrm{Cov}[A, B]. \tag{4.2}$$

One way to compute these correlations would be to compute the covariance matrix of the predictors using our dataset. However, this would amount to incorporating information from the data to our prior, which could in turn lead us to overestimate the accuracy of our model. However, while this bias affects our test error estimate, we are confident that it does not invalidate the insights we get from comparing the estimates computed using different values of our parameters. Furthermore, in practice, one would expect that the user would use (in 2-D) eight rather than just 4 electrodes, and that the information from the additional four electrodes, selected to circumscribe the region already analysed by the four electrodes, would compensate this bias.

In an experiment, we included all six voltages from each of the three injection patterns in the feature matrix, adding independent noise to each. This resulted in a diminution of the actual variance of each voltages as compared to the chosen value of ν^2, since it was equivalent to drawing several realizations of each voltage, as e.g. $V_5 = V_3 - V_1 = V_4 + V_6$. It made results harder to interpret, so we kept the initial model.

This is interesting to note that none of the previous studies on the topic included a noise model for the boundary measurements. Their conclusions were thus that the anisotropy of the electrical conductivity was one of the main factors that made EIT difficult to apply on

CFRP, without further exploring this relationship. Hence, the noise model and its analysis here is a significant contribution of this research.

4.2 Results from the whole dataset

4.2.1 Impact of noise and algorithms comparison

In this section, we compare the prediction performances of the algorithms presented in Chapter 3. Figure 4.3 shows the error rates against the noise's standard deviation for all algorithms, electrode shifts and anisotropy level. It is the same graph as Figure 4.1, except that this time we considered the complete dataset. We used 800 samples for training and 200 for testing, 10 times. Note that in this graph the maximum noise standard deviation is 5% of the voltage magnitude, while in Figure 4.1 it ranged from 0 to 10%. As expected, prediction errors are more frequent. Delaminations with size close to the chosen threshold $a = 6.75$ mm are harder to classify, since even a good estimation of their size can lead to a misclassification.

Figure 4.3 confirms the trends we first observed in Figure 4.1. On one hand, in the case of high anisotropy, one observes better accuracies when little noise is added, but prediction performance worsens quickly when noise crosses a threshold depending on anisotropy. On the other hand, when λ is small the error rates are disappointingly far from zero on noiseless data but remain relatively stable as we add more noise.

From Figure 4.3, one can clearly see that:

- k-NN is always worse;
- SVM and random forests perform roughly as well.

We will henceforth only show results using SVM and random forests.

4.2.2 Number of training samples required

One of the goals of this study is to determine how many training samples are needed to achieve near optimal performance. Figure 4.4 shows the error rates as a function of the number of training samples, with $E_{sh} = 0$. The number of test samples is kept fixed at 200.

We observe from the graphs it is clear that the asymptotic value of the error rate, i.e. the misclassification rate as $N_{\text{tr}} \to \infty$, is almost reached when $N_{\text{tr}} = 800$. In fact, little to no progress is made, in general, between 200 and 800. We should remind the reader at this point that the subject of the analysis is a 2D laminate with a single lamina. Hence the values of N_{tr} where the curve flattens in Figure 4.4 may not be meaningful for real world conditions.

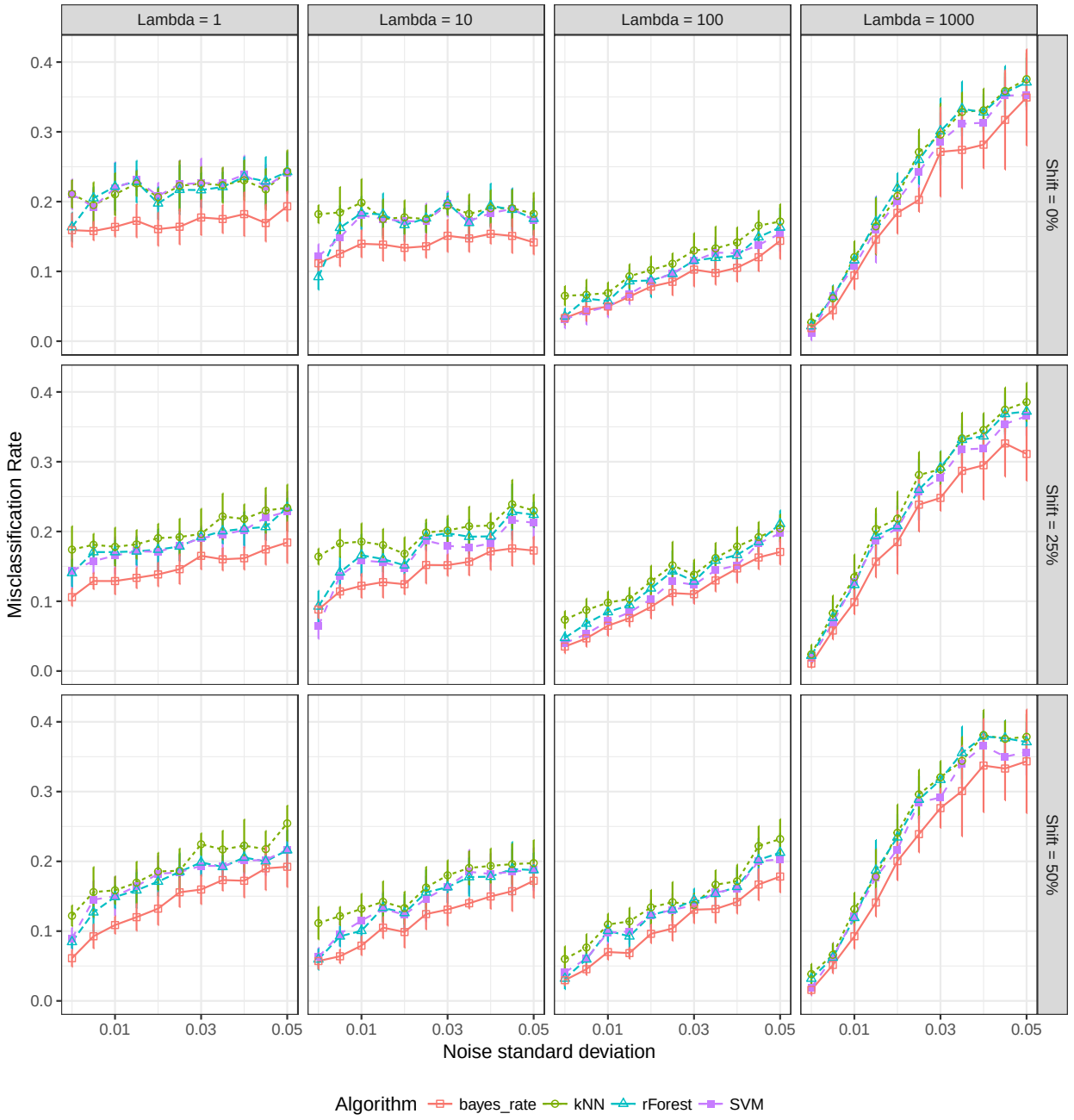

Figure 4.3 Misclassification rate as a function of the noise standard deviation, 800 training data, 200 test data, repeated 10 times.

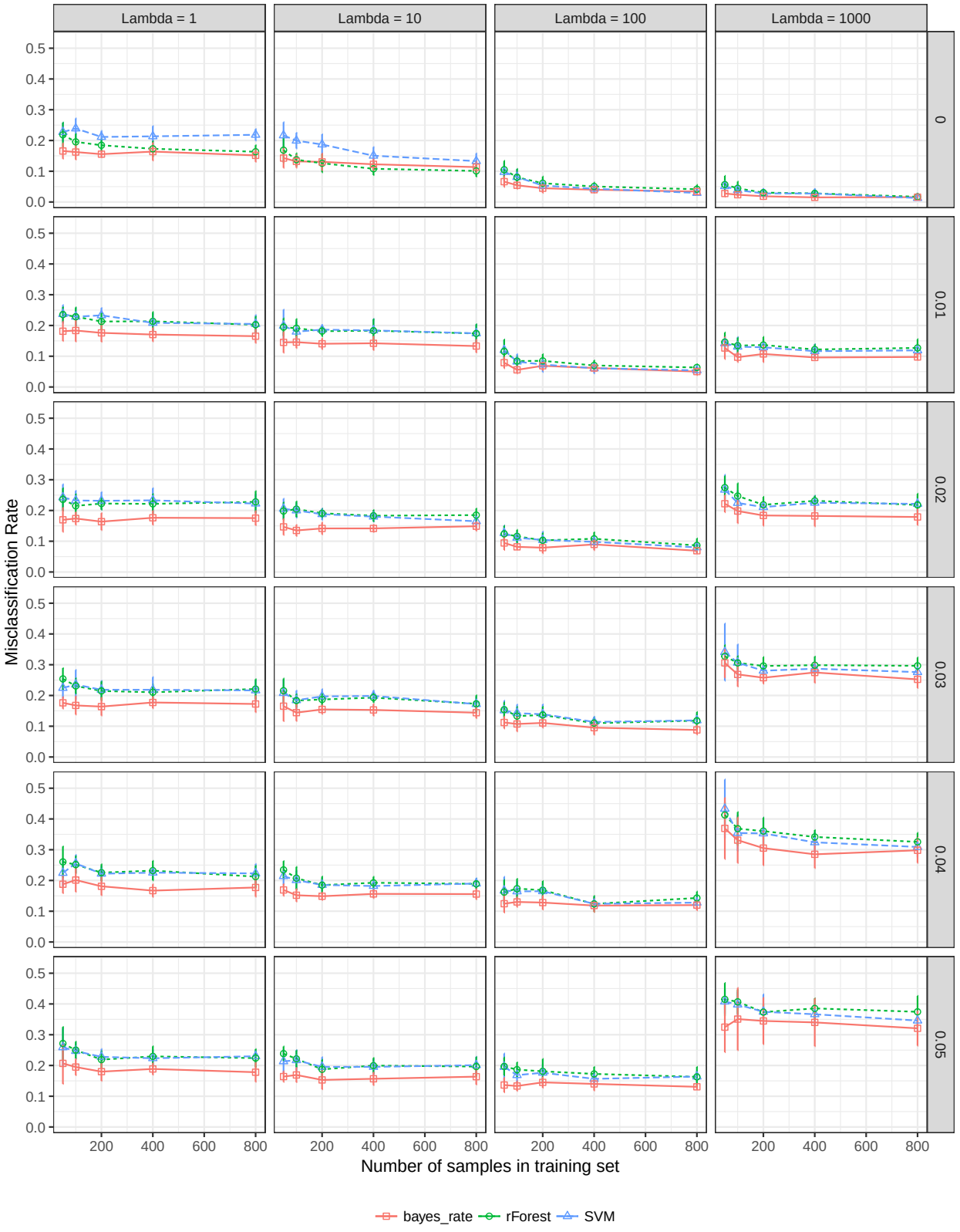

Figure 4.4 Misclassification rate against the number of training samples. 200 test data, repeated 10 times.

As adding one dimension to the geometry could increase that value, we may postulate that we would need at least 200 samples in the 3D case, thus providing a lower bound on the amount of work necessary for detection.

4.2.3 Comparison of different electrode settings

In order to better compare the different electrode settings, the error rates obtained with each set-up are superimposed in Figure 4.5.

When the anisotropy is extremely high, i.e. for $\lambda = 1,000$, the different electrode set-ups yield similar results. On the contrary, in the isotropic case, the electrode set-up seems to have an impact: the set-up with $E_{sh} = 50\%$ provides better predictions, especially when ν is close to zero. Recall that in Figure 4.2 we could see that delaminations were harder to detect when they were located far from the electrodes, but that this relationship between damage location and prediction performance became less obvious as λ grew. As the influence of the relative location with respect to the electrodes vanishes, so does the influence of the positioning of the latter, which explains the results shown in Figure 4.5.

4.2.4 Comparison with cavity detection

Angelidis and Irving [2] remarked that damaged areas consist of fiber breaks and intra laminar cracks as well as inter laminar delaminations. The goal of this section is to find if prediction results on data taking into account the added effect of fiber breakage are significantly different from those obtained with data simulating the effect of through-thickness conductivity change only. To achieve that, we plotted the error rates obtained with cavity data, as described in Section 2.4.2, against those obtained with delamination data, as described in Section 2.4.1. For the sake of clarity, we only show the error rates obtained with the SVM algorithm. Results are displayed in Figure 4.6. As expected, it is significantly easier to detect a cavity than a delamination, except when $\lambda = 100$. The high error rates observed in Figure 4.3 for small λ and near zero E_{sh}, which we interpreted as being caused by the incapability to detect delamination located far away from the electrodes, disappear when delamination are replaced by cavities.

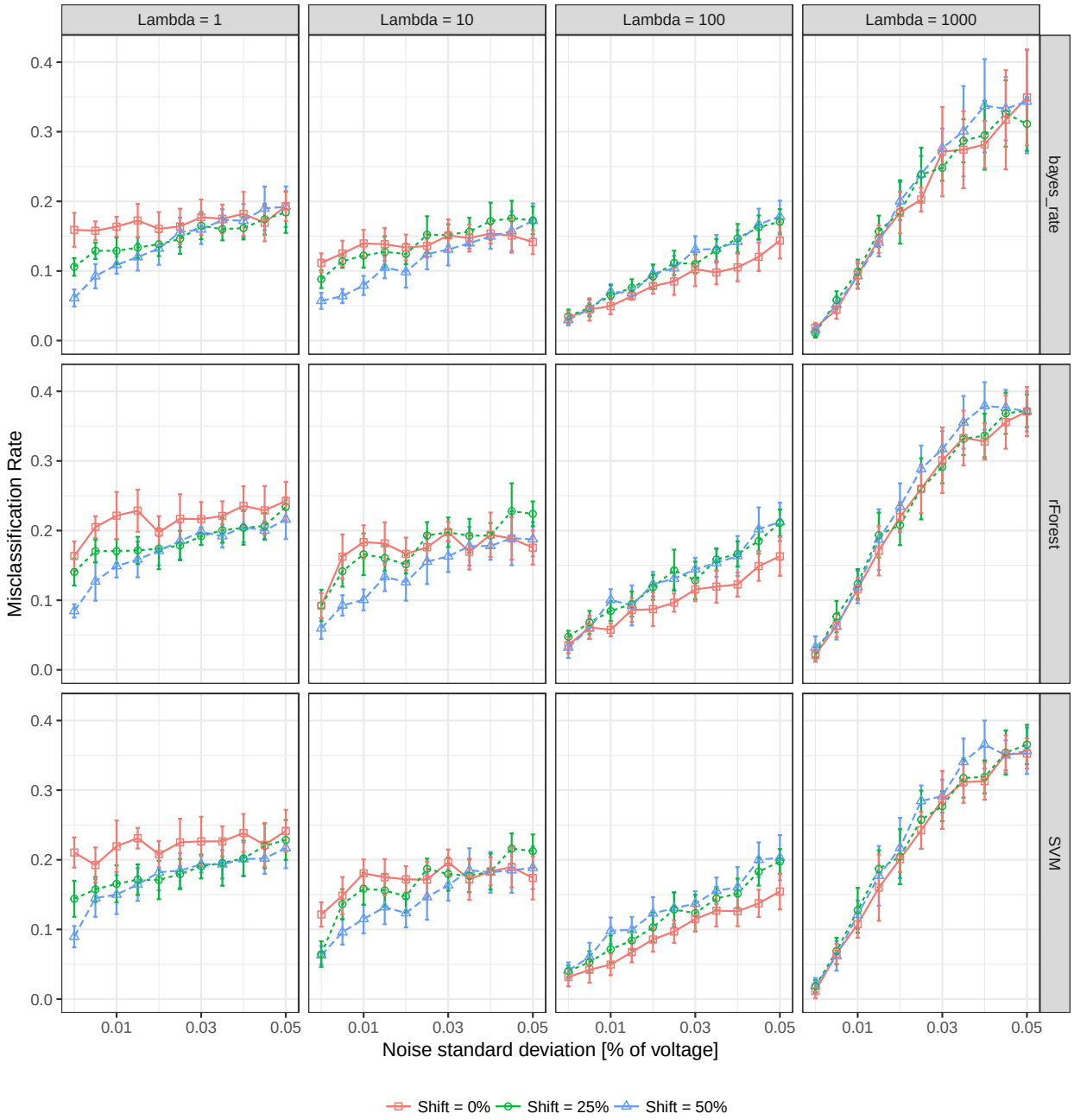

Figure 4.5 Comparison of the error rates obtained with different electrodes settings. 800 training data, 200 test data, repeated 10 times.

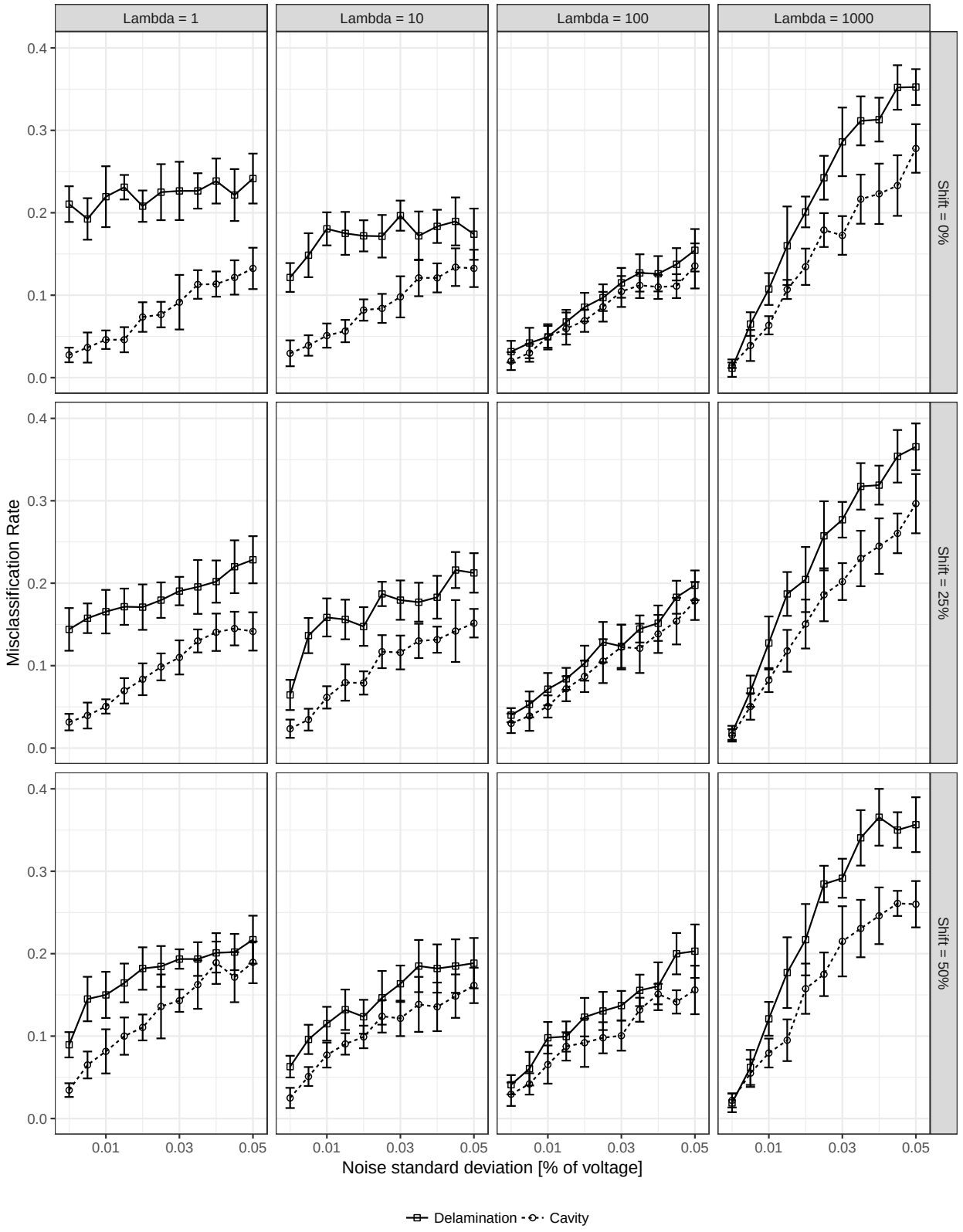

Figure 4.6 Comparison of the SVM error rate for detection of delaminations and cavities. 800 training data, 200 test data, repeated 10 times.

CHAPTER 5 CONCLUSION

5.1 Study synthesis

In this study, we described a methodology that consists of using machine learning algorithms to infer the presence of damage in CFRP from boundary voltage measurements. We implemented the CEM to generate data samples and used standard machine learning algorithms to solve the inverse problem. The SVM and random forest algorithms yielded similar performances, while the k-NN algorithm was constantly outperformed. As our estimate of the Bayes error was not significantly smaller, using other state-of-the-art machine algorithms would probably not help us with reducing the error.

Since we observed that at least 200 samples are needed to provide an error rate "close enough" to its asymptotic value, we postulate that hundreds are necessary to achieve good accuracy on three-dimensional composite. Our cavity experiment confirmed our intuition that delaminations are harder to detect than cavities, as the latter obstruct both in-plane and through-thickness conductivity, while delaminations affect through-thickness conductivity only.

By using machine learning algorithms for a classification tasks, rather than attempting to predict a continuous variable, i.e. delamination sizes, we were able to visualize the dependence of prediction performance on damage location more efficiently. First, this enabled us to confirm that the damage cases that are the hardest to detect are the ones located the farther from the electrodes, as it had been reported in numerous papers. More importantly, studying the joint effect of anisotropy, electrode positioning, and noise on the prediction performance allowed us to uncover a link between anisotropy and geometry that had not been previously identified. We initially suspected that our results would lead us to define an upper bound on the conductivity ratios which makes the inverse identification feasible. Instead, we observed that anisotropy might actually help us improve predictions when the material is thin. In other words, our results seem to indicate that unless the electrode density is very high, i.e. the electrode spacing is in the same order of magnitude as the material thickness, the electrical anisotropy may help engineers to extract more reliable predictions from EIT. Another way to state this is that thinner materials require a greater anisotropy in order to balance the length scales (depth of composite versus distance between electrodes) and thereby improve detection in regions farther away from the electrodes. This observation leads us to recommend doing further research on the relationship between material geometry, anisotropy level and optimal electrode spacing.

5.2 Limitations

The use of exclusively synthetic data is not enough to conclude that the proposed method is efficient in real life situations. Nevertheless, the majority of the approximations introduced in the development of the model, notably in the mathematical characterization of delamination, lead to overestimates of its predictive power. Hence our conclusions overall do not allow us to conclude that EIT detection is impossible. In fact, past studies of EIT for composites have come to similar conclusions for the same range of parameters we considered.

Nevertheless, the studies we undertook indicate that certain properties of EIT could be leveraged to improve accuracy and reliability, maybe even to the point of making this approach feasible. We therefore cautiously encourage further study of this problem be undertaken, particularly with appropriately prepared samples of composites.

5.3 Future work

This general statement attempts to highlight the fact that there are still some discrepancies between how EIT works in composites and how they are modelled numerically. In particular, the experimental set-up, the choice of electrodes, and especially the possibility of using electrodes on both sides of the composite, should be carefully evaluated. So far, there does not seem to be a consensus on the form in which EIT could be implemented in the field, say in specific applications in the aerospace industry.

Highly resistive ply-ply interfaces should be taken into account in the modeling of the forward problem. In this work, we assumed that the conductivity was homogeneous in the through-thickness direction, but in reality it is equal to that of the transverse direction inside each plies but considerably lower in the matrix rich ply-ply interfaces. Those interfaces are likely to increase both the data generation cost and the difficulty of inverse inference.

A reasonable hypothesis is that prediction results would be slightly better if using not only four electrodes (or eight in 3D) but also surrounding grid electrodes. Also, including a full frequency model would probably increase detectability of delaminations, based on experimental results we have seen. In order to get a deeper understanding of the joint effect of geometry, electrode positioning, and anisotropy on damage detection, one could add a "material thickness" parameter to our methodology. Ideally, we want to find a description of the optimal electrode spacing as a function of geometrical and conductivity parameters.

Another issue is the bias due to our noise model. Future work should focus on improving the noise model, e.g. by taking voltage correlations into account. One could also simulate

the presence of minor material imperfections using noise in order to decrease the cost of data generation. This would be faster than solving the forward problem multiple times for small (benign) delamination.

One of the important conclusions of our study is that the predictions from different machine learning algorithms are relatively close, with a slight preference for more highly non-linear approaches such as SVM with radial basis function and random forests. In any case, our studies did not seek the optimal implementation of our chosen machine learning algorithms, and there is still some room for improvement of detection if the hidden parameters of the algorithm were optimized for the chosen task.

BIBLIOGRAPHY

[1] Hirotogu Akaike. Information theory and an extension of the maximum likelihood principle. In *Selected papers of hirotugu akaike*, pages 199–213. Springer, 1998.

[2] N. Angelidis and P. E. Irving. Detection of impact damage in CFRP laminates by means of electrical potential techniques. *Composites Science and Technology*, 67(3):594–604, 2007.

[3] David C. Barber and Brian H. Brown. Applied potential tomography. *Journal of Physics E: Scientific Instruments*, 17(9):723, 1984.

[4] Joakim Beck, Ben Mansour Dia, Luis FR Espath, Quan Long, and Raul Tempone. Fast bayesian experimental design: Laplace-based importance sampling for the expected information gain. *arXiv preprint arXiv:1710.03500*, 2017.

[5] Abdessalem Benammar, Redouane Drai, and Abderrezak Guessoum. Detection of delamination defects in cfrp materials using ultrasonic signal processing. *Ultrasonics*, 48 (8):731–738, 2008.

[6] Charly Billet, Serge Prudhomme, Marc Laforest, Kenan Kergrene, and Augustin Schmidt. Electrical impedance tomography. Technical report, Polytechnique Montreal, 2017.

[7] Leo Breiman. *Classification and regression trees*. Routledge, 1984.

[8] Leo Breiman. Bagging predictors. *Machine learning*, 24(2):123–140, 1996.

[9] Leo Breiman. Random forests. *Machine Learning*, 45(1):5–32, Oct 2001. ISSN 1573-0565.

[10] Corinna Cortes and Vladimir Vapnik. Support-vector networks. *Machine learning*, 20 (3):273–297, 1995.

[11] Thomas Cover and Peter Hart. Nearest neighbor pattern classification. *IEEE transactions on information theory*, 13(1):21–27, 1967.

[12] David R. Cox. The regression analysis of binary sequences. *Journal of the Royal Statistical Society. Series B (Methodological)*, pages 215–242, 1958.

[13] Eugene Demidenko, Andrea Borsic, Yuqing Wan, Ryan J Halter, and Alex Hartov. Statistical estimation of eit electrode contact impedance using a magic toeplitz matrix. *IEEE Transactions on Biomedical Engineering*, 58(8):2194–2201, 2011.

[14] Bradley Efron. *The jackknife, the bootstrap, and other resampling plans*, volume 38. SIAM, 1982.

[15] Bradley Efron and Robert J. Tibshirani. *An introduction to the bootstrap*. CRC press, 1994.

[16] M Endrizzi, BIS Murat, P Fromme, and A Olivo. Edge-illumination x-ray dark-field imaging for visualising defects in composite structures. *Composite Structures*, 134:895–899, 2015.

[17] Luis Waldo Escalona-Galvis, Paulina Diaz-Montiel, and Satchi Venkataraman. Optimal electrode selection for electrical resistance tomography in carbon fiber reinforced polymer composites. *Materials*, 10(2):125, 2017.

[18] Luis Waldo Escalona-Galvis, Paulina Diaz-Montiel, and Satchi Venkataraman. Optimum electrode configurations for two-probe, four-probe and multi-probe schemes in electrical resistance tomography for delamination identification in carbon fiber reinforced composites. *Journal of Composites Science*, 2(2):29, 2018. ISSN 2504-477X.

[19] Alexandre Fouchard, Stéphane Bonnet, Lionel Hervé, and Olivier David. Flexible numerical platform for electrical impedance tomography. *COMSOL Conference in Grenoble*, 2015.

[20] Engr Ekundayo Gbenga. Using non-destructive testing for the manufacturing of composites for effective cost saving: A case study of a commercial prepreg CFC. *International Journal of Materials Engineering*, 6(2):28–38, 2016.

[21] Victor Giurgiutiu. *Structural Health Monitoring of Aerospace Composites*. Academic Press, 2015.

[22] Ian Goodfellow, Yoshua Bengio, and Aaron Courville. *Deep Learning*. MIT Press, 2016.

[23] Jacques Hadamard. Sur les problemes aux derive espartielles et leur signification physique. *Bulletin of Princeton University*, 13:1–20, 1902.

[24] T Hastie, R Tibshirani, and J Friedman. *The Elements of Statistical Learning*. New York: Springer, 2 edition, 2009.

[25] Geoffrey E Hinton and Ruslan R Salakhutdinov. Reducing the dimensionality of data with neural networks. *science*, 313(5786):504–507, 2006. doi: 10.1126/science.1127647.

[26] Atsushi Iwasaki and Akira Todoroki. Statistical evaluation of modified electrical resistance change method for delamination monitoring of cfrp plate. *Structural Health Monitoring*, 4(2):119–136, 2005.

[27] Gareth James, Daniela Witten, Trevor Hastie, and Robert Tibshirani. *An introduction to statistical learning*, volume 112. Springer, 2013.

[28] Daniel C. Kammer. Sensor placement for on-orbit modal identification and correlation of large space structures. *Journal of Guidance, Control, and Dynamics*, 14(2):251–259, 1991.

[29] Ron Kohavi. A study of cross-validation and bootstrap for accuracy estimation and model selection. In *Ijcai*, volume 14, pages 1137–1145. Stanford, CA, 1995.

[30] Z. Li, A. Haigh, C. Soutis, A. Gibson, R. Sloan, and N. Karimian. Detection and evaluation of damage in aircraft composites using electromagnetically coupled inductors. *Composite Structures*, 140:252–261, 2016.

[31] Andy Liaw, Matthew Wiener, et al. Classification and regression by randomforest. *R news*, 2(3):18–22, 2002.

[32] David Meyer and FH Technikum Wien. Support vector machines. *R News*, 1(3):23–26, 2001.

[33] T. M. Mitchell. *Machine Learning*. McGraw-Hill International Editions. McGraw-Hill, 1997. ISBN 9780071154673.

[34] Paulina Diaz Montiel. *Exploration on surrogate models for inverse identification of delamination cracks in CFRP composites using Electrical Resistance Tomography*. PhD thesis, San Diego State University, 2016.

[35] J. Mueller and S. Siltanen. *Linear and Nonlinear Inverse Problems with Practical Applications*. Society for Industrial and Applied Mathematics, Philadelphia, PA, 2012.

[36] Frank Rosenblatt. The perceptron: a probabilistic model for information storage and organization in the brain. *Psychological Review*, 65(6):386, 1958.

[37] Arthur L. Samuel. Some studies in machine learning using the game of checkers. *IBM Journal of research and development*, 3(3):210–229, 1959.

[38] Ruediger Schueler, Shiv P Joshi, and Karl Schulte. Damage detection in cfrp by electrical conductivity mapping. *Composites Science and Technology*, 61(6):921–930, 2001.

[39] Gideon Schwarz et al. Estimating the dimension of a model. *The annals of statistics*, 6 (2):461–464, 1978.

[40] Lakshmi Selvakumaran, Quan Long, Serge Prudhomme, and Gilles Lubineau. On the detectability of transverse cracks in laminated composites using electrical potential change measurements. *Composites Structures*, 121:237–246, 2015.

[41] Erkki Somersalo, Margaret Cheney, and David Isaacson. Existence and uniqueness for electrode models for electric current computed tomography. *SIAM Journal on Applied Mathematics*, 52:1023–1040, 1992.

[42] Albert Tarantola. *Inverse problem theory and methods for model parameter estimation*, volume 89. siam, 2005.

[43] Akira Todoroki. Effect of number of electrodes and diagnostic tool for delamination monitoring of graphite/epoxy laminates using electric resistance change. *Composites Science and Technology*, 61(13):1871–1880, 2001.

[44] Akira Todoroki, Miho Tanaka, and Yoshinobu Shimamura. Measurement of orthotropic electric conductance of CFRP laminates and analysis of the effect on delamination monitoring with an electric resistance change method. *Composites Science and Technology*, 62:619–628, 2002.

[45] Akira Todoroki, Miho Tanaka, and Yoshinobu Shimamura. High performance estimations of delamination of graphite/epoxy laminates with electric resistance change method. *Composites Science and Technology*, 63(13):1911–1920, 2003.

[46] Kagan Tumer and Joydeep Ghosh. Estimating the Bayes error rate through classifier combining. In *Proceedings of the 13th International Conference on Pattern Recognition, 1996*, volume 2, pages 695–699. IEEE, 1996.

[47] Xiaojun Wang and D. D. L. Chung. Sensing delamination in a carbon fiber polymer-matrix composite during fatigue by electrical resistance measurement. *Polymer Composites*, 18(6):692–700, 1997.

[48] Hadley Wickham et al. Tidy data. *Journal of Statistical Software*, 59(10):1–23, 2014.

[49] Ruizhen Yang and Yunze He. Polymer-matrix composites carbon fibre characterisation and damage inspection using selectively heating thermography (seht) through electromagnetic induction. *Composite Structures*, 140:590–601, 2016.

[50] Yi Zou, LPSG Tong, and Grant P Steven. Vibration-based model-dependent damage (delamination) identification and health monitoring for composite structures—a review. *Journal of Sound and vibration*, 230(2):357–378, 2000.